

Final Report for the Long Term Space Astrophysics Grant "The Study of Clusters of Galaxies and Large Scale Structures"

The Long Term Space Astrophysics Grant "The Study of Clusters of Galaxies and Large Scale Structures", NAGW-2508, has been completed. Many research projects have been initiated and completed under support of this program. The results are summarized below.

The work on the ROSAT Deep Survey has been successfully completed. A number of interesting results have been established within this joint MPE, Cal Tech, JHU, ST ScI, ESO collaboration. First, a very large fraction, 70-80 percent, of the X-ray background has been directly resolved into point sources. We have derived a new log N-log S for X-ray sources and have measured a source density of 970 sources per square degree at a limiting flux level of 10^{-15} erg $s^{-1}cm^{-2}$ (0.5-2.0 keV). Care was taken in these studies to accurately model and measure the effects of sources confusion. This was possible because of our observing strategy which included both deep PSPC and HRI observations.

From a complete ROSAT Deep Survey sample of 50 objects to a flux limit of $5.5 \cdot 10^{-15}$ erg $s^{-1}cm^{-2}$ (0.5-2.0 keV) we have established that 78 percent of the XRB are AGN, 8 percent are groups, 2 percent are galaxies and 6 percent are stars, with 6 percent remaining unidentified. This is the highest fraction of identified objects in a high sensitivity X-ray survey to date. No evidence of a population of narrow emission line galaxies has been established but some evidence for the evolution of low luminosity AGN (Seyfert galaxies) has been reported.

The work on the ROSAT All Sky Survey Northern Cluster Survey has been substantially concluded but the publication of the list has been held up by the need to analyze newly re-calibrated data. This should result in publication over the next year. During the past year we have submitted a paper to the Astrophysical Journal which utilized a sample of clusters originally selected from the ROSAT All-sky survey at redshifts greater than 0.3. This sample was studied with ASCA to determine temperature and luminosity. This sample was then compared to a low redshift sample and the density of the universe, q_0 , was measured. The result is that q_0 is consistent with an open universe, a result that is consistent with the recent observations on Type Ia supernova by Perlmutter et al (1997) and Garnavich et al (1998).

In the last year of the project we initiated work on a number of aspects of the Origins program and in particular I participated in the design and development of the Next Generation Space Telescope. A number of scientific papers emerged including an analysis of the use of a sub-scale NGST to perform a large area, high sensitivity near infrared survey, calculations demonstrating how the NGST could discover and characterize a large number of exo-zodiacal discs, and a separate paper discussing how a small interferometer could be used for both zodiacal disc studies and discovery of large Jupiter like planets.

I include below a bibliography of papers which report on work supported in part by the LTSA program. In addition, I attach four recent papers written with partial support from this program.

Bibliography

- Burrows, C. J., Burg, R., Giacconi, R., "Optical Grazing Incidence Optics, and Its Application to Wide Field X-ray Imaging", 1992 Ap. J., 392, 760.
- Huchra, J., and Burg, R., "The Spatial Density of Active Galactic Nuclei. I. The Density of Seyfert Galaxies and Liners", 1992, Ap. J., 393, 90.
- Giacconi, R. and Burg, R., "The X-ray Background: Past, Present and Future", 1992, The X-ray Background, Barcons, X and Fabian, A., eds., Cambridge Univ. Press.
- McLean, B. and Burg, R., "Optical Identification of X-ray Sources from Digitized Sky Survey Plates", 1992, McGillivray and Thompson, eds., Digitized Sky Surveys, Kluwer.
- Burg, R., Giacconi, R., Huchra, J., MacKenty, J., McLean, B., Geller, M., Hasinger, G., Marzke, R., Schmidt, M., and Trumper, J. "Discovery of Intermediate Redshift Galaxy Clusters in the ROSAT NEP Field", 1992, *Astronomy & Astrophysics*, 259, L9.
- Burg, R., Cavaliere, A., and Menci, N. "The Soft X-ray Background and Galaxy Clusters", 1993, Ap. J., 404, L55.
- Hasinger, G., Burg, R., Giacconi, R., Hartner, G., Schmidt, M., Trumper, J. and Zamorani, G., "A Deep X-ray Survey in the Lockman Hole", 1993, *A.&A.*, 275, 1.
- Giacconi, R. and Burg, R. "The Northern ROSAT Cluster Surveys", 1993, P.A..S.P.conference series vol 51, eds.: G. Chincarini and T. Maccacaro.
- Burg, R., Giacconi, R., Forman, W.R., and Jones, C., "The X-ray Luminosity Functions for Abell Clusters", 1994, Ap.J., 422, 37.
- Henry, J. P., I. M. Gioia, H. Boehringer, R. G. Bower, U.G. Briel, G. H. Hasinger, A.Aragon-Salamanca, F. J. Castander, R. S.Ellis, J. P. Huchra, and R. Burg, B. McLean, and R. Giacconi, "RX1759.4+6638: An X-ray Selected Quasar at a Redshift of 4.320", 1994, *AJ*, 107, 1270..
- Lattanzi, M., Hershey, J., Burg, R., Taff, L., Holfeltz, S., Bucciarelli, B., Evans, I.N., Gilmozzi, R., Pringle, J., and Walborn, N., "The Hubble Space Telescope Fine Guide Sensor Interferometric Observation of the Core of 30 Doradus", 1994, *Ap.J. Letters*, 427, L21.

- McLean, B.J., Böhringer, H., Burg, R., Giacconi, R., H, J.P. and Voges, W., "Optical Identification of ROSAT All-sky Survey Galaxy Cluster Candidates", 1994, Astronomy from Wide-field Imaging, eds.; H. MacGillivray et al., IAU.
- Henry, J.P., Gioia, I.M., Huchra, J.P., Burg, R., McLean, B., Boehringer, H., Bower, R.G., Briel, U.G., MacGillivray, H, and Cruddace, R.G., "Groups of Galaxies in the ROSAT North Ecliptic Pole Survey", *Ap.J.* 1995, 449, 422.
- Maccacaro, T., Wolter, A., McLean, B.J., Gioia, I.M., Stocke, J.T., Della Ceca, R., Burg, R. and Faccini, R., "The Einstein Observatory Einstein Extended Medium Survey III. The Atlas of Optical Finding Charts", 1994, *Astronomical Letters*, 29, 267.
- Ford, H., Bely, P., Bally, J., Crocker, J., Dopita, M., Tilley, J., White, R., Allen, R., Bartko, F., Brown, R., Burg, R., Burrows, C., Clampin, M., Harper, D., Illingworth, G., McCray, R., Meyer, S., Mould, J., and Norman, C., 1994, *SPIE* Vol. 219, Advanced Technology Optical Telescopes V.
- Rosati, P. Roberto Della Ceca, Richard Burg, Colin Norman, Riccardo Giacconi, "A First Determination of the Surface Density of Galaxy Clusters at very low X-ray fluxes", 1995, *Ap.J. Letters*, 20 May.
- Bely, P.Y., Ford, H.C., Burg, R., Petro, L., White, R., and Bally, J., "POST: Polar Stratospheric Telescope", 1995, *Space Science Reviews*.
- Bower, R.G., Hasinger, G., Castander, F.J., Aragon-Salamanca, A., Ellis, R.S., Gioia, I.M., Henry, J.P., Burg, R., Huchra, J.P., Bohringer, H. Buriel, U.G., and McLean, B., "The ROSAT North Ecliptic Pole Survey", *MNRAS*, 1996, 281, 59.
- Hasinger, G., Burg, R. Giacconi, R., Schmidt, M., Trumper, J., Zamorani, G., "The ROSAT Deep Survey I - X-ray Sources in the Lockman Field", 1998 *A&A* 329,482.
- Schmidt, M., Hasinger, G., Gunn, J., Schneider, D., Burg, R. Giacconi, R., Lehmann, I., MacKenty, J., Trumper, J., Zamorani, G., "The ROSAT Deep Survey II - Optical Identification of X-ray Sources in the Lockman Field", 1998 *A&A* 329,495.
- Burg, R., Bely, P.Y., Petro, L., Gay, J., Rabbia, Y, Baudoz, P., Redding, D., "Searching for Exo-zodiacal Discs with a Rotation Shearing Interferometer on NGST, 1998, in "Science with NGST", ASP Conference Series, Vol. 133, 214, E.P. Smith and A. Koratkar, eds..
- Burg, R., Bely, P.Y., Madau, P., McLean, B., Noll, K., and Stiavelli, M., "NIRAS: A Proposal for a Near Infrared Astronomical Survey Mission", 1998, in "Science

with NGST", ASP Conference Series, Vol. 133, 221, E.P. Smith and A. Koratkar, eds..

Bely, P.Y., Burg, R., Petro, L., Gay, Wade, L., Beichman, C., J., Rabbia, Y, Baudoz, P., Perrin, J.-M., "The Exo-zodiacal Disc Mapper", 1998, accepted for publication in "Experimental Astronomy".

Rines, K., Forman, W., Pen, U., Jones, C., and Burg, R., "Determination of q_0 from the Cluster Gas Mass Fraction, 1998, Ap.J., submitted.

Science with the NGST
ASP Conference Series, Vol. 133, 1998
E. P. Smith and A. Koratkar, eds.

NIRAS: A Proposal for a Near Infrared Astronomical Survey Mission

R. Burg

Johns Hopkins University, Baltimore, MD 21218

P. Bély, Piero Madau, Brian McLean, Keith Noll and Massimo Stiavelli

Space Telescope Science Institute, 3700 San Martin Dr., Baltimore, MD 21218

Abstract.

We propose that a 1/10 scale model of NGST equipped with extensive technical instrumentation, and a near infrared and mid infrared camera be launched to L2 to serve as a technical validation of the overall concept while providing useful science in support of NGST's scientific program. After a 3 month period for technical investigations, the spacecraft would be used for one year to perform wide angle surveys in the near and mid infrared.

1. Introduction

A precursor mission to NGST is being discussed as a way to validate the new technologies being developed. This raises a number of questions. If a precursor mission were launched 3-5 years before NGST launch how would this knowledge be used? Is it necessary for technical success? Can a scientifically useful mission be constructed? We have given these questions some thought and have concluded that a well thought out precursor mission could be extremely valuable both technically and scientifically. The result of our analysis is our concept for a Near Infra-red Astronomical Survey (NIRAS) mission which we describe hereafter.

2. NIRAS Mission Architecture

The goal of NIRAS is to perform a complete system level test of NGST while carrying out a significant scientific program. The scientific program would be wide-angle surveys in both the near infrared (NIR) and mid infrared (MIR) bands down to limiting fluxes that are far in excess of past or ongoing large angle surveys. NIRAS would be a 1/10th scale model of NGST with the following characteristics:

- *optics*: 0.8 meter primary mirror, diffraction limited at 5 microns for a pixel scale of about 0.5 arcsec in the near infrared;
- *instruments*: one 4k × 4k NGST NIR camera for field of 0.75 × 0.75 sq. degree and one 1k × 1k MIR camera viewing the same field as the

NIR camera through a dichroic filter; the MIR camera would be critically sampled at 19 micron;

- *technical instrumentation* fully instrumented for testing models and have at least 3 months of engineering tests before commencing science investigation;
- *type of mission*: class C (no redundancy, no special selection of parts);
- *orbit* L2 orbit (same as NGST in order to test operations);
- *launch date*: no later than the middle of NGST phase B;
- *science mission*: approximately a 1 year science mission that would survey 5,000 square degrees, in six passbands (3 NIR and 3 MIR) with exposure time per field of 900 seconds.

A single fifteen minute exposure reaches a limiting sensitivity of 0.5 microjanskys at 2.5 microns and 10 microjanskys at 20 microns. These values are over a hundred-thousand times more sensitive than IRAS, over a thousand times more sensitive than 2MASS, 10-20 times more sensitive than WIRE and comparable to the Sloan Survey (which is in the visible). It reaches the sensitivity limit of the most capable pointed observatories such as SIRTf but can efficiently survey at least an eighth of the sky, in six passbands per year. The key technology which will enable this advance is the development of large format NIR/MIR detectors for the NGST project.

3. Technical Justification

A precursor mission would be a full dress rehearsal and can be justified for a number of technical and programmatic reasons. First we must recognize that NGST is a new type of observatory, our experience database does not really apply. Secondly, NGST is a "fragile" mission, it has flexible structures and little protection (e.g. thin, flexible sunshield rather than traditional telescope tube and aperture door). Thirdly, NGST operations are fully integrated with the hardware - they should be tested together (especially for safe modes). Finally, no servicing, no recovery, but the use of risk management to mitigate the need to recover from off nominal situations is a guiding principle for NGST. What is interesting about the above list is that the same attributes that make NGST less expensive to build make it more vulnerable, and makes the need for a fully integrated test environment such as the proposed NIRAS mission critical. Simulation and modeling are crucial for NGST success, but as the HST primary mirror figure error and the recent Ariane 5 failure have shown, this approach can only go so far.

A precursor mission must be affordable to fit into the NGST program. It probably can not be justified if it is more than about 1/10th of the NGST cost. Potential cost saving strategies could include:

- use of NGST systems and engineering models, particularly cameras, deployment mechanisms and primary mirror (both hardware and software);
- limited use of NGST ground segment and operations;

It
for co
the m
Light
a shut
from a
that th
traditi
and 5
million

4. S

A wid
NGST
the No

A
compl
micron
band i
than 2
1. We
planne
most s
genera
Digita

A
to NG
which
such a
use of
confus
where
time.
if Ω is
fact, v
arcmin
percer
missic
much
likelih
would
A
tronor

- and no traditional science team.

It seems reasonable that this mission could be achieved at MIDEX costs for construction, about \$50 M. Based on the studies for NGST, we estimate the mass at 200-300 kg. This mass is sufficiently low that a Taurus or Delta Light launch vehicle could insert it into a L2 orbit. Another possibility would be a shuttle launch together with a small booster or probably the most optimum from a cost point of view a piggyback launch with another mission. We believe that this survey mission could be operated at very low cost. There would be no traditional science team, and we estimate that only 5 FTE/year for operations and 5 FTE/year for cataloging would be needed for a cost of approximately \$2 million for the one year science mission.

4. Science Program

A wide angle survey at these sensitivities would offer important support for NGST science but would not be a substitute for or a necessary pre-condition for the NGST mission.

A 5000 square degree survey in 3 NIR bands and 3 MIR bands can be completed in a year of observation. These bands might be at 1, 2.5 and 5 microns in the NIR and at 8, 12, and 20 microns in the MIR. The 1 micron band is interesting because it offers the possibility of identifying redshift greater than 2.5 galaxies photometrically. Limiting sensitivities are shown in Figure 1. We have also plotted the limiting sensitivities of overlapping existing and planned surveys (Beichman 1997). As can be seen, NIRAS is capable of the most sensitive wide-angle surveys to date and considerably extends the current generation of NIR/MIR surveys. NIRAS will complement SIRTf, the Sloan Digital Sky Survey, and the new generation of ground-based observatories.

A wide angle survey at these sensitivities would be a significant complement to NGST especially by discovering rare objects (less than 1 per square degree) which would be followed up spectroscopically by NGST. NGST could perform such a survey over a wide area of the sky, but this would be a very inefficient use of that observatory. As long as a telescope is background limited and not confusion limited then the relevant figure of merit for survey efficiency is $A \Omega t$, where A is telescope area, Ω is the telescope field of view, and t is the survey time. If t is kept fixed then it can be seen that telescope area can be reduced if Ω is increased proportionally to keep the survey figure of merit constant. In fact, with its 0.75×0.75 square degree field of view as compared to the 4×4 arcmin² field of view of NGST, NIRAS is slightly more efficient (about ten percent more) than NGST for doing surveys at these flux levels. In a one year mission NIRAS can survey 5,000 thousand square degrees for objects that the much more powerful NGST can then study in greater detail allowing for the likelihood of significant new discoveries. As can be seen from Figure 2, NIRAS would outperform all existing and planned surveys.

A wide-angle survey would contribute significant data in a number of astronomical fields such as:

- *Search for Kuiper Belt objects:* Starting with the object 1992QB1, more than 36 objects with diameters of approximately 100 km have been discovered in orbits 30-40 AU from the Sun. The discovery rate suggests that

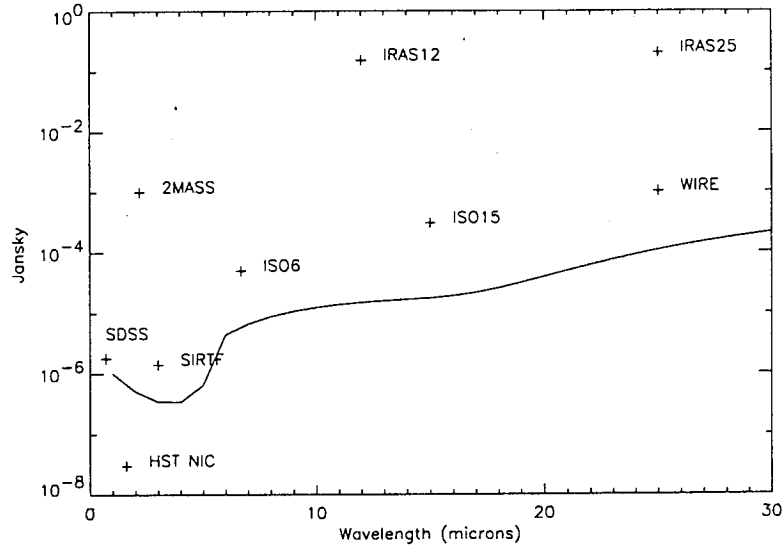


Figure 1. Sensitivity of NIRAS as a function of wavelength compared to other existing or planned surveys

the density of objects within 10 degrees of the ecliptic and with $V \leq 24$ is of order 10 per square degree. The proposed instrument would therefore be able to discover about 36000 such objects by selecting candidates from the multi-color survey. Given that at their typical distance they would be moving at about 1.7 arcsec/day, the discovery method of choice would be to re-image the ecliptic after one day and, possibly, one week. The availability of a large number of these objects would help us clarifying their spatial distribution, orbital properties and nature: whether they are captured objects or an independent family of solar system objects.

- *Search for Brown Dwarfs:* Brown dwarfs are extremely important objects both for their potential impact on the structure of the Milky Way (since they could contribute a significant fraction of the MW mass) and for improving our knowledge of the low mass end of the stellar luminosity function. An all sky survey sensitive to atmospheric methane and/or water bands would make it feasible to assemble an unprecedented data set. Old brown dwarfs are particularly hard to identify since they are dim. However, they contain precious information on stellar cooling processes at low temperatures. A brown dwarf like GL 229B could be imaged at a distance 10 times larger, i.e. out to about 60 pc. Suitable absorption bands exist in the region 1 to 5 microns. The band between 4 and 5 microns appears particularly promising for detecting brown dwarfs since, in this band, they should be brighter than a black body. In order to get a clear cut identification, the 4-5 microns filter could be coupled with a narrower filter at 3.3 microns to measure the depth of the methane band.

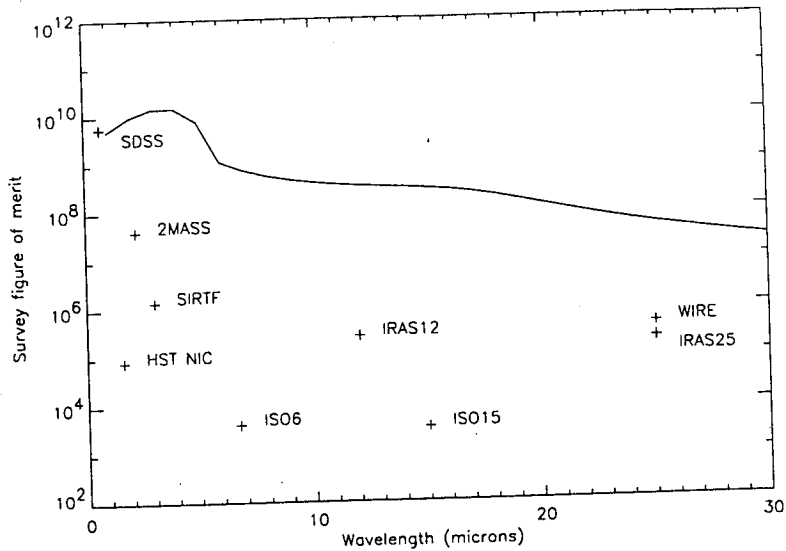


Figure 2. Survey figure of merit as a function of wavelength for NIRAS and other existing or planned surveys. The figure of merit is defined as the ratio of the total sky area in degrees observed during the mission lifetime to the survey sensitivity in Janskys

- *Search for high redshift galaxies:* With a sensitivity of better than a microjansky at 2.5 microns, NIRAS is capable of discovering large number of high redshift galaxies. In particular, NIRAS will be able to find galaxies which because of their very high luminosity are rare. NIRAS would be particularly important for determining if old stellar populations exist in high luminosity, high redshift galaxies. These type of systems might be very rare but if they exist at all they would severely constrain models for galaxy evolution. Old populations may be discovered through the migration of the H+K break through the NIR passbands of NIRAS. Young population galaxies at high redshift may be discovered by combining this survey with a high sensitivity visible survey such as the Sloan Digital Sky Survey. Our estimates are very approximate, do not include K-corrections, and are bounded by investigating two values of q_0 (0 and 0.5). They use a no evolution model and are normalized by using the Hubble Deep Field estimate of 4 ($z \geq 2$) galaxies per square arcminutes at an AB limiting magnitude of 25. We conclude that NIRAS would potentially discover over 10^5 galaxies at $z > 3$ and between a few hundred and a few thousand at $z > 4$. These very high luminosity systems could then be studied in great detail spectroscopically by NGST.

The above programs are just examples of fields which would benefit from a high sensitivity survey. Interesting astronomical studies could be made in many other fields including large scale structures, AGN and stellar discs. It is clear that NGST science would benefit from the wide angle survey which NIRAS can

wavelength compared

otic and with $V \leq 24$ is
 ument would therefore
 lecting candidates from
 al distance they would
 method of choice would
 ossibly, one week. The
 ould help us clarifying
 ature: whether they are
 r system objects.

remely important objects
 of the Milky Way (since
 MW mass) and for im-
 stellar luminosity func-
 methane and/or water
 recedented data set. Old
 nce they are dim. How-
 cooling processes at low
 be imaged at a distance
 e absorption bands exist
 4 and 5 microns appears
 s since, in this band, they
 to get a clear cut identi-
 with a narrower filter at
 e band.

supply in much the same way that the large ground base telescopes have profited from the wide angle surveys performed by Schmidt telescopes.

5. Conclusions

From the technical and cost points of view, NIRAS capitalizes on the technical breakthroughs accomplished for NGST: ultra lightweight optics; passively cooled optics; fully integrated active optics mounted in flexible, lightweight, structures; operation at L2; and instruments with very large format, low noise, infrared detectors. NIRAS would provide a substantial risk reduction for the NGST program by testing at the full system level the basic NGST design. It would be fully instrumented to carry out engineering tests and would spend its first 3-6 months carrying out important NGST validation. Finally, it would carry out a significant scientific program that would contribute to the success of NGST and perhaps most significantly, build the partnership between the scientific and technical teams that are necessary for the success of contemporary astronomical missions.

References

- Beichman, C. 1997, "New Horizons from Multiwavelength Surveys, Proceedings of the 179th symposium of the International Astronomical Union", eds., B.J. McLean, D. A. Golombek, J. J. E. Hayes, H. E. Payne, Kluwer Academic Publishers

1. I
The E
ous fa
1997).
redshi
presen
(Song
occurr
galaxie
stars,
the un

1.1.
As in
beginn
proble
resides
the gal
for tho
several
story a

1.2. ()
The Ne
window
generat
mode o

Science with the NGST
ASP Conference Series, Vol. 133, 1998
E. P. Smith and A. Koratkar, eds.

Searching for Exo-zodiacal Discs with a Rotation Shearing Interferometer for NGST

R. Burg

Johns Hopkins University, Baltimore, MD 21218

P. Y. Bély, L. Petro

Space Telescope Science Institute, 3700 San Martin Drive, Baltimore, MD 21218

J. Gay, Y. Rabbia, P. Baudoz

Observatoire de la Côte Azur, Avenue Copernic, F-06130 Grasse

D. Redding

Jet Propulsion Laboratory, 4800 Oak Grove Drive, Pasadena, CA 91109

Abstract. The detection of exo-zodiacal discs is an important step in the NASA program for the detection of exo-solar planet, in particular, the detection of earth-like planets. We show that that by incorporating a nulling interferometer NGST would be very well suited to study exo-zodiacal disks in nearby stars. Over 400 stars could be surveyed and at least 40 could be resolved such that structural parameters on the 2-3 AU scale could be measured. This can be done within the existing optical NGST design but demands a wavefront RMS error less than $\lambda/100$ at $10\mu\text{m}$ in order to assure a wavefront cancellation of 1000.

1. Introduction

The direct detection and characterization of earth-like planets is one of the main goals of NASA's *Origins* program. A keystone mission of that program, the "Terrestrial Planet Finder Array" or TPFA, is a large nulling interferometer which in its current design consists of four 1.5 meter telescopes on a 70-100 meter baseline (Beichman, 1996). However, a number of scientific and technical achievements must be accomplished before such a major instrument can be built. One of the most significant scientific questions that needs to be answered is the existence, intensity and orientation of potential zodiacal dust disks in candidate extra-solar systems.

The luminosity of the dust in the inner 10 AU of the Solar System is of order $10^{-7}L_{\odot}$, whereas the luminosity of Earth is $5 \times 10^{-10}L_{\odot}$. In the infrared, at $10\mu\text{m}$ the flux of the Zodiacal Dust is $F_{ZD} \simeq 1 \times 10^{-4}F_{\odot}$ and the flux of Earth is $F_{\oplus} = 5 \times 10^{-7}F_{\odot}$. Therefore, whether in the visible or in the infrared, methods for the detection of extrasolar planets have to contend not only with the glare of the adjacent star but also with that of the enveloping zodiacal dust. Nulling

interfe
planet
zodiac
of ma,
will b
than c
edge c
T
missio
durati
numbe
This i
the int
more t
A
imum
the nu
tion p
For sp
be blir
A
depend
set of
sampl
zodiac
In
a rota
moder
the pla

2. In

Since s
flux de
if the
zodiac
At 10μ
wavele
of app
Tr
the lig
drawba
typical
0.25 ar
which
linear c
If
an inte
closer t
ferome

interferometers efficiently cancel the flux of the adjacent star. However, as the planets are not resolved, a substantial zodiacal dust signal is still detected. This zodiacal dust signal, as suggested by the Solar System example, may be orders of magnitude brighter than terrestrial planets. Detection of an earth-like planet will become difficult if the signal from the exo-zodiacal disk is much brighter than our own zodiacal disk, or if the exo-zodiacal dust disk is viewed close to edge on.

This is a critical issue because of the small number of stars that a given mission can investigate. The first restriction comes from the limited mission duration and sky coverage. The integration times required are fairly long and the number of stars that can be observed during a mission's lifetime is not generous. This is exacerbated by the incomplete sky coverage due to sun constraint on the interferometer: because of the elliptic heliocentric orbit proposed for TPF-A, more than one third of the sky will not be accessible.

A related problem arises from the fixed baseline of the interferometer. Maximum response from a potential planet occurs when its angular separation from the nulled parent star is such that it is at a peak of the fringe pattern. For detection purposes, this can be adjusted to some extent by changing the wavelength. For spectroscopic analysis, however, an interferometer with a given baseline will be blind to certain discrete angular separations.

A consequence of these limitations is that the success of the TPF-A critically depends upon tuning the interferometer design and the observing program to a set of preselected candidate stars. It will therefore be critical to survey a large sample of stars for the presence, orientation, gross structure and brightness of zodiacal dust disks.

In what follows we show that with the addition of a modest instrument, a rotation shearing interferometer, NGST could perform such a survey at a moderate cost in observation time, and could thus significantly to the success of the planet finding mission

2. Interferometric Coronagraph

Since surface brightness is an invariant with distance, the amount of exo-zodiacal flux detected by a telescope is the same as the flux of our own zodiacal light if the exo-zodiacal disc emits at the same intensity and spectrum as our own zodiacal disc. Our solar system's zodiacal disc extends out to a radius of 3 AU. At $10\mu\text{m}$ the integrated flux is $\sim 10^{-4}F_{\odot}$, as compared to $\sim 10^{-7}F_{\odot}$ if the wavelength of observation is $0.5\mu\text{m}$. Cancellation of the primary star by a factor of approximately 1000 is necessary to detect the exo-zodiacal disc.

Traditionally, Lyot stop coronagraphs have been employed to both block the light from the central source and to suppress wide-angle scattering. The drawback to this approach is that all the light within 3-5 airy disc radii is typically blocked. In the case of NGST, which has its first Airy disc radii at 0.25 arcsecond at $\lambda = 10$ microns, this corresponds to a scale of ≈ 1 arcsecond which is much too large for the detailed study of exo-zodiacal discs (a disc of linear dimension 3 AU at 10 parsec subtends an angle of 0.3 arcsecond).

If instead of blocking the light with a physical stop, the light is cancelled by an interferometric technique, then it is possible to perform observations much closer to the bright point source. In fact, this is what a rotation shearing interferometer does. The heart of the system is a beam combiner which splits the

Rotation

ive, Baltimore,

130 Grasse

Madena, CA 91109

important step in planet, in particular, at by incorporating suited to study exo-be surveyed and at eters on the 2-3 AU the existing optical less than $\lambda/100$ at 1000.

planets is one of the on of that program, nulling interferometer telescopes on a 70-100 scientific and technical instrument can be built. to be answered is the dust disks in candidate

Solar System is of order 0. In the infrared, at and the flux of Earth is the infrared, methods ot only with the glare zodiacal dust. Nulling

with roof prisms (or dihedral mirrors) to flip the beams and with one arm of the interferometer constructed out of the plane. This allows the *S*-component of one beam and the *P*-component of the other beam to be rotated by the required 180° while keeping the complementary component of each beam in their original states. This approach is simple in that only flat mirrors are necessary but it has two drawbacks. First, since each reflection is 45° and the *S* and *P* waves are not reflected in a symmetric manner polarization-dependent attenuation and anomalous phase delays can cause the beams to become unbalanced. Second, the constructive interference exit port coincides with the entrance port and is thus inaccessible. The design proposed by Gay and Rabbia is another modification to the Michelson interferometer. All optical paths lie in the plane. One of the interferometer arms uses only reflections on flat mirrors, while the other uses a "cat's eye", a two mirror system which functions as a unit magnification relay and has an intermediary focus at the secondary mirror. The (achromatic) 180° phase shift in this arm occurs as the rays pass through focus (Gouy 1890, Born and Wolf, 1980). All angles are kept small, *S* and *P* components are reflected in a symmetric manner, and both the constructive and destructive ports are accessible, the constructive port being useful for monitoring and controlling optical path differences. This optical design uses the beamsplitters in a symmetrical way. The light from each telescope uses the beamsplitter once in transmission and once in reflection. This gets around the problem of fabricating a beamsplitter which is exactly 50%/50% over a large bandpass. The nulling combiner proposed by Gay and Rabbia has been proven in the laboratory and is presently undergoing testing on a telescope at the Observatoire de la Côte d'Azur. A cancellation level down to a few percent has already been achieved and further improvements are expected.

For an NGST instrument, a cancellation of about 1000 to 1 should be achievable assuming that the optics wavefront error is less than $\lambda/100$ at $\lambda = 10\mu\text{m}$ and that tilt error is less than 2.5 milliarcseconds. This last condition is close to the current guiding specification for the core science instruments and should easily be met using a specific guiding system locked on the candidate star in the proposed interferometric coronagraph

3. Number of Observable Exo-zodiacal Discs

Using a detailed simulation of an interferometric coronagraph response that we have developed for a dedicated space mission proposal (Bély et al 1997) and a model of the exo-zodiacal light based on the IRAS data (Good 1994), we have calculated the exposure time required to detect a zodiacal disk with an intensity similar to ours around each star in the solar neighborhood. We used the data from the Gliese catalog (Gliese and Jahreiss, 1989) which extends to 50 parsecs and excluded all known or suspected binary star (since companions are not nulled by the interferometer and would preclude any detection of the much fainter zodiacal disk). The calculation was done assuming an overall transmission of 50% for the optics; a temperature of 50 Kelvin for the passively cooled telescope mirrors, a coating emissivity of 3%, a quantum efficiency of 65% for the detector and a signal-to-noise ratio per sample point of 10. The solar system zodiacal background was calculated for each star based on its ecliptic latitude. Star leakage was included, the star diameter being estimated from its absolute magnitude, spectral class and radiation law, and assuming a line of sight jitter

erferometer
elow (draw-
e, the other
ie construc-
the number
. Since the
is results in
o telescopes
wo arms (to
e reflection co-
pletely sym-
missions at
e 180° phase
romatic and
acteristics of

respect the other
in order to create
ty. Hence the 180°
obtained by chang-
or monochromatic
ombiner which we
novel design devel-
(, 1996) and named
earing interferome-
) the 180° rotation
lson interferometer

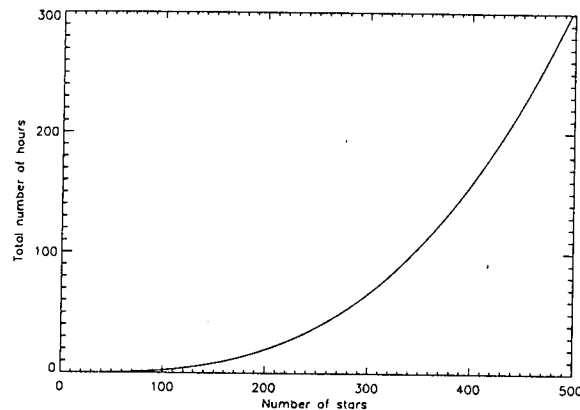


Figure 2. Total Total number of hours required to detect and map exo-zodiacal disks as a function of the desired star sample. The average signal-to noise ratio per sampling point is 10 and only non binary stars are included.

of 2.5 milliarcseconds. Finally we assumed that the null on axis would not be better than 10^{-4} due to residual wavefront errors, and intensity or polarization mismatch.

The results are summarized in Figure 2. We find that approximately 400 stars can be measured in about 100 hours. This is to be compared to the few tens of stars measurable on the ground with the Keck or a similar number observable with an HST visible band coronagraph.

4. Conclusion

A rotation shearing coronagraph would add a significant scientific capability to NGST and we suggest that further study be done on integrating one into the science instrument package. The proposed design is compact, insensitive to errors due to polarization because of its high degree of internal symmetry, and has both the constructive and destructive port fully accessible. Finally, it is easily modified to measure the absolute wavefront error on the pupil. With this capability NGST would have a dedicated wavefront sensor and this may enhance the overall efficiency of fine-tuning the observatory optics.

References

- Beichman, C. A., 1996, A road map for the exploration of neighboring planetary systems, JPL Pub 96-22
- Bély, Petro, Burg, Beichman, Gay, Baudoz, Rabbia, Perrin, The Exo-zodiacal disk mapper: a space interferometer to detect and map zodiacal disks around nearby stars, 1997, submitted to Experimental Astronomy
- Born, M, and Wolf, E., 1980, Principles of Optics, Pergamon Press

Gay J. and
 Gliese W. a
 of Ne
 Heide
 Good, J., 19
 T.N.
 D. Gr
 Gouy, L.G.,
 Roddier, F.,
 Shao M., 198
 Telesc
 Shao, M., an

- Gay J. and Y. Rabbia, 1996, C.R. Acad. Sci., Paris, 322, serie II b, 265
- Gliese W. and Jahreiss, H., 1989, Preliminary Version of the Third Catalogue of Nearby Stars", (electronic version), Astronomisches Rechen-Institut, Heidelberg
- Good, J., 1994, in IRAS Sky Survey Atlas; Appendix G, eds. S.L. Wheelock, T.N. Gautier, J. Chillemi, D. Kester, H. McCallon, C. Oken, J. White, D. Gregorich, F. Boulanger. J. Good, T. Chester
- Gouy, L.G., 1890, C.R. Acad. Sci., Paris, 110, 1251
- Roddier, F., Roddier, C. and Demarcq, J., 1978, J. Optics, 9, 145.
- Shao M., 1989, in Proc. NASA/STScI Workshop on the Next Generation Space Telescope, ed P. Bély, C. J. Burrows and G. Illingworth, 160
- Shao, M., and Colavita, M., 1992, A&A Reviews, 30, 457



d map
verage
y stars

ould not be
polarization

imately 400
the few tens
r observable

ic capability
ing one into
t, insensitive
l symmetry,
e. Finally, it
pupil. With
nd this may

cing planetary

Exo-zodiacal
zodiacal disks
ronomy

ss

A&A manuscript no.

(will be inserted by hand later) 1998 A&A 329, 482

Your thesaurus codes are:

03(04.19.1;12.04.2;13.25.2)

NAGW-2508

ASTRONOMY
AND
ASTROPHYSICS
15.9.1997

The ROSAT Deep Survey

I. X-ray sources in the Lockman Field

G. Hasinger¹, R. Burg², R. Giacconi³, M. Schmidt⁴, J. Trümper⁵, G. Zamorani^{6,7}

¹ Astrophysikalisches Institut Potsdam, An der Sternwarte 16, 14482 Potsdam, Germany

² Johns Hopkins University, Baltimore, MD 21218, USA

³ European Southern Observatory, Karl-Schwarzschild-Str. 1, 85748 Garching bei München, Germany

⁴ California Institute of Technology, Pasadena, CA 91125, USA

⁵ Max-Planck-Institut für extraterrestrische Physik, Karl-Schwarzschild-Str. 2, 85740 Garching bei München, Germany

⁶ Istituto di Radioastronomia del CNR, via Gobetti 101, I-40129 Bologna, Italy

⁷ Osservatorio Astronomico, via Zamboni 33, I-40126 Bologna, Italy

Received 12 May 1997; accepted 4 Aug 1997

Abstract. The ROSAT Deep Survey in the *Lockman Hole* is the most sensitive X-ray survey performed to date, encompassing an exposure time of 207 ksec with the PSPC and a total of 1.32 Msec with the HRI aboard ROSAT. Here we present the complete catalogue of 50 X-ray sources with PSPC fluxes (0.5–2 keV) above $5.5 \times 10^{-15} \text{ erg cm}^{-2} \text{ s}^{-1}$. The optical identifications are discussed in an accompanying paper (Schmidt et al., 1997). We also derive a new $\log(N)$ - $\log(S)$ function reaching a source density of $970 \pm 150 \text{ deg}^{-2}$ at a limiting flux of $10^{-15} \text{ erg cm}^{-2} \text{ s}^{-1}$. At this level 70–80% of the 0.5–2 keV X-ray background is resolved into discrete sources. Utilizing extensive simulations of artificial PSPC and HRI fields we discuss in detail the effects of source confusion and incompleteness both on source counts and on optical identifications. Based on these simulations we set conservative limits on flux and on off-axis angles, which guarantee a high reliability of the catalogue. We also present simulations of shallower fields and show that surveys, which are based on PSPC exposures longer than 50 ksec, become severely confusion limited typically a factor of 2 above their 4σ detection threshold. This has consequences for recent claims of a possible new source population emerging at the faintest X-ray fluxes.

Key words: surveys – cosmology: diffuse radiations – X-rays: galaxies

1. Introduction

The study of the X-ray background (XRB), originally discovered 35 years ago (Giacconi et al., 1962), with imaging X-ray telescopes has progressed rapidly in the last few years. After a pioneering start with deep Einstein exposures (Giacconi et al., 1979, Griffiths et al., 1983, Hamilton et al., 1991), ROSAT deep survey observations were able to resolve the majority of the soft XRB into discrete sources (Hasinger et al., 1993, hereafter H93). First deep imaging exposures with ASCA have extended these studies into the hard X-ray band (Inoue et al. 1996, Cagnoni et al., 1997). The X-ray band is one of the few regions of the electromagnetic spectrum, where the integrated emission of discrete sources, summed over all cosmic epochs, is dominating the celestial emission. The XRB therefore provides a strong constraint for cosmological evolution models (see e.g. Comastri et al., 1995; Zdziarski 1996). In order to understand the populations contributing to the X-ray background and their cosmological evolution it is necessary to obtain complete optical identification of the sources detected in X-ray deep surveys. The majority of optically identified X-ray sources at faint fluxes are active galactic nuclei (AGN), i.e. QSOs and Seyfert galaxies with broad emission lines (Shanks et al., 1991; Boyle et al., 1993; Bower et al., 1996; Page et al., 1996). Using the large samples of X-ray selected AGN now becoming available, their luminosity function and its evolution with redshift can be studied in detail (Boyle et al., 1995; Page et al., 1996; Jones et al., 1996). The current models, which are based on pure luminosity evolution, predict that the broad-line AGN contribute only 30–50% to the soft X-ray background and much less to the hard X-ray background. Postulating a large population of faint, intrinsically ab-

astro-ph/9709142 15 Sep 1997

sorbed AGN, some models predict a much larger fraction of the soft XRB, and possibly all of the hard XRB as due to AGN (see e.g. Comastri et al., 1995; Zdziarski 1996).

There are, however, reports that at the faintest X-ray fluxes a new population of X-ray active, but optically relatively normal narrow-emission line galaxies (NELG) start to dominate the X-ray counts, and could ultimately contribute the majority of the XRB (Georgantopoulos et al. 1996, Griffiths et al. 1996, McHardy et al., 1997). These claims are based on deep ROSAT PSPC surveys which – as we will show – start to be severely confusion limited at the faintest fluxes. Care has therefore to be taken to assess the systematic position errors and misidentification likelihood at faint fluxes. In our own deep survey identification work we have therefore taken measures to minimize confusion and to increase the reliability of the X-ray catalogue. We restricted the sample to X-ray fluxes well above the detection threshold at a reliable flux level derived from detailed simulations. Secondly, we invested massive amounts of ROSAT HRI time to cover our deepest survey field in the Lockman Hole, this way minimizing position errors and confusion. In this paper (paper I) we describe the derivation of the X-ray source catalogue in the Lockman Hole. Section 2 gives a summary of the observations, Sect. 3 describes the new maximum likelihood (ML) crowded-field detection algorithm developed for deep X-ray survey work, Sect. 4 discusses the necessary astrometric corrections for ROSAT PSPC and HRI images and Sect. 5 gives the final source catalogue. The verification of the analysis procedure through simulations and the derivation of a final $\log(N)$ - $\log(S)$ function are discussed in Sect. 6 and a discussion of the results is given in Sect. 7. The complete optical identification of the X-ray source catalogue is described in *paper II* (Schmidt et al., 1997) and deep VLA radio observations of the field are discussed by deRuiter et al. (1997).

2. Observations

The data presented here consists of all observations of the ROSAT Deep Survey accumulated in the period 1990–1997 in the direction of the Lockman Hole, which is one of the areas on the sky with a minimum of the galactic Hydrogen column density; N_H is roughly $5 \times 10^{19} \text{ cm}^{-2}$ in this field (Lockman et al., 1986). Table 1 gives a summary of these observations. Specifically, a total exposure time of 207.41 ksec was accumulated with PSPC (Pfeffermann and Briel 1992) pointings centered at the direction $RA(2000) = 10^h 52^m$, $DEC(2000) = 57^\circ 21' 36''$. These data have been partially presented in H93. For the PSPC data all good time intervals selected by the ROSAT standard analysis (SASS; Voges 1992) have been analysed. The individual datasets obtained in different semesters, which are affected by residual erratic aspect errors of order 10 arcsec, were all shifted to a common celestial reference system using preliminary optical identifications. A PSPC

image with a pixel size of 5 arcsec, covering the most sensitive area of the field of view (FOV), with a radius of ~ 20 arcmin, has been accumulated in the standard PSPC “hard” energy band 0.5–2 keV (pulseheight channel 52–201). This choice optimizes the angular resolution of the PSPC and the signal to noise ratio for the detection of faint extragalactic sources. It is also relatively insensitive to neutral hydrogen absorption column densities below $\sim 10^{21} \text{ cm}^{-2}$. For the calculation of hardness ratios we additionally analysed the PSPC data in the “soft” band and further subdivided the hard band into two: H1 and H2. Details about the energy bands are given in Table 2. Fig. 1a shows a contour plot of the PSPC image in the hard band.

The same area has also been covered by a set of raster scan observations with the ROSAT HRI (David et al., 1996). A total of ~ 100 pointings of roughly 2 ksec exposure each, has been placed on a regular grid with a step size of ~ 2 arcmin. The HRI FOV has a size of roughly 36×36 arcmin. The inner, most sensitive part of the field, where the off-axis blur of the telescope can be neglected, has a radius of roughly 8 arcmin. The raster scan step size is much smaller than the HRI FOV, thus the resulting exposure covers the survey area smoothly, with a rather homogeneous point spread function (PSF) across the field. The total exposure time accumulated for the raster scan is 205.50 ksec, comparable to the PSPC pointing. The individual HRI pointing data provided by the ROSAT Standard Analysis System SASS (Voges 1992) have been merged into a single mosaïque, after separate astrometrical solutions have been applied to each dataset, in order to correct for residual boresight and scale factor errors in the HRI data (see below). The HRI raster image has been accumulated in the restricted pulseheight channel range 1–9, which significantly reduces the detector background with a minimum loss ($\sim 7\%$) of cosmic X-ray photons (David et al., 1996). Using this channel selection, the HRI is sensitive to cosmic X-ray photons in the full ROSAT energy range 0.1–2.4 keV. Fig. 1b shows the resulting HRI raster scan image on the same scale as the PSPC data.

From Fig. 1 it is obvious, that the HRI raster scan, although having significantly higher resolution, is not nearly as sensitive as the PSPC observation which, however, is reaching the confusion limit (see below). In an attempt to reach an unconfused sensitivity limit comparable or deeper than the PSPC exposure, at least in a substantial fraction of the PSPC FOV, we performed an ultradeep HRI exposure of 1 Msec in a single pointing direction. The ROSAT attitude system shows residual pointing errors on the order of several arcsec, which can lead to a corresponding positional shift of the resulting image (see below). Uncorrected aspect errors can also lead to a substantial ellipticity of the HRI images of point sources (David et al., 1996), thus reducing resolution and sensitivity. To some degree these aspect errors can be corrected for, if one or

Table 1. Observation Summary

Start Date	End Date	Instrument	Exp. [s]
1990 Apr 16	1991 May 21	PSPC	67989
1991 Apr 25	1991 May 5	HRI raster	86778
1991 Oct 25	1991 Nov 2	PSPC	24327
1991 Oct 27	1991 Nov 9	HRI raster	116635
1992 Apr 15	1992 Apr 24	PSPC	66272
1992 Apr 18	1992 Apr 18	HRI raster	2082
1992 Nov 29	1992 Nov 29	PSPC	2082
1993 Apr 26	1993 May 9	PSPC	46740
1994 Oct 21	1994 Nov 7	HRI	106565
1995 Apr 15	1995 May 11	HRI	294483
1995 Oct 26	1995 Nov 27	HRI	200358
1996 May 1	1996 May 29	HRI	319590
1997 Apr 15	1997 Apr 28	HRI	191094

more bright optically identified X-ray sources are present in the image. In order to allow this procedure, we selected a pointing direction for the ultradeep HRI exposure, which is inside the PSPC field of view, but shifted about 10 arcmin to the North-East of the PSPC center, this way covering a region containing about 10 relatively bright X-ray sources known from the PSPC and the HRI raster scan. The ultradeep HRI exposure is centered at the direction $RA(2000) = 10^h 52^m 43^s$, $DEC(2000) = 57^\circ 28' 48''$. In some situations the automatic ROSAT HRI standard analysis system is too conservative in rejecting time intervals with supposedly high background. In particular using the background-optimized HRI channel range 1-9, we found an optimum point-source detection sensitivity including all exposure intervals with good attitude data. For the ultradeep survey we therefore selected events using a custom made procedure after having joined the SASS accepted and rejected event files. This resulted in a net observing time of 1112.09 ksec, a gain of $\sim 20\%$ compared to the SASS products. The individual datasets obtained in different semesters were shifted to the same reference system as the PSPC data, using preliminary optical identifications. The HRI image in the pulseheight channel range 1-9 is shown in Fig. 1c on the same scale as the PSPC image, which makes the shift to the North-East quite apparent.

3. Detection algorithm

The images in Fig. 1 have been analysed using an improved version of the interactive analysis system EXSAS (Zimmermann et al. 1994). The first steps of the detection procedure, i.e. the local detect algorithm LDETECT, the bicubic spline fit to the background map and the map detection algorithm MDETECT have been described in H93. The detection threshold of these algorithms has been set at a very low likelihood value so that the resulting list of possible source positions contains several hundred spurious detections. This position list has then been fed

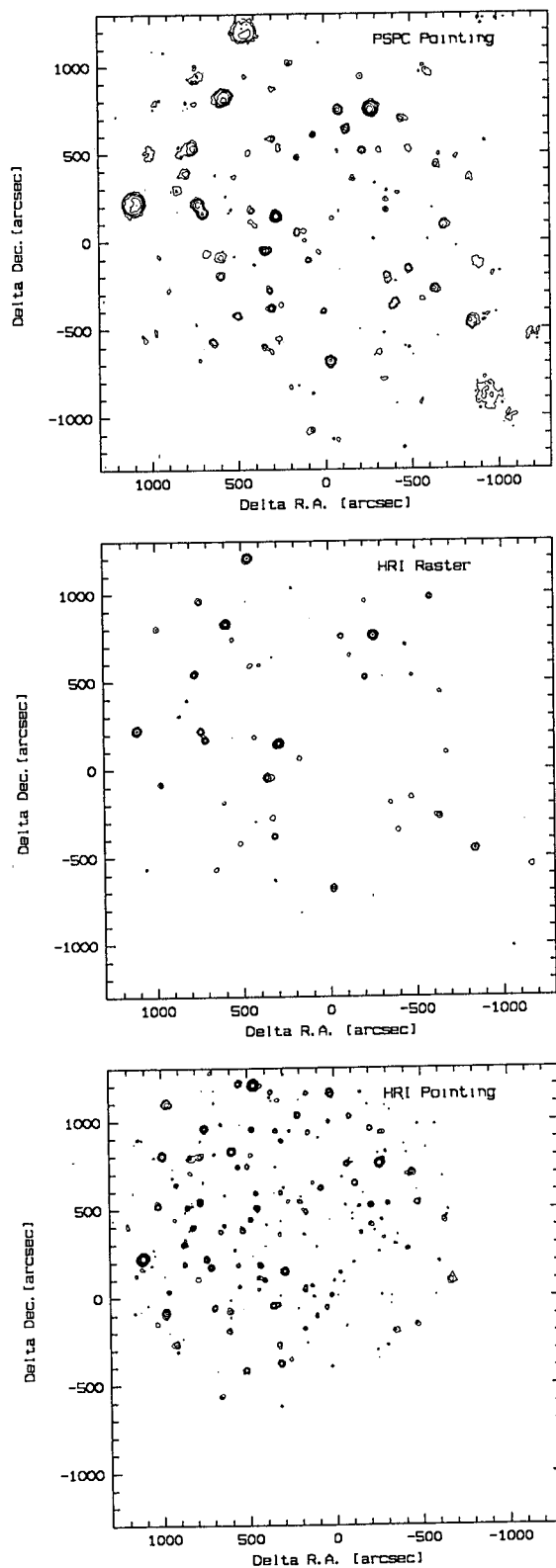


Fig. 1. ROSAT Deep Survey images in the Lockman Hole: (a) PSPC 207 ksec pointing, (b) HRI 205 ksec raster scan and (c) HRI 1112 ksec pointing. The images are all centered at the PSPC pointing direction (see text).

into the “multi-ML” crowded field detection and parameter estimation algorithm first described by Hasinger et al. (1994a). This method, which has been implemented into EXSAS, works on binned image data and fits superpositions of several PSF profiles on top of an external background to sections of the data (typically sub-images of arcmin size). Best-fit positions and normalizations are obtained by maximizing the likelihood statistic \mathcal{L} (Cash 1979) or, correspondingly, by minimizing the quantity

$$S = -2\ln\mathcal{L} = -2 \sum_{i,j} (Y_{mod}(i,j) - N(i,j)\ln Y_{mod}(i,j)) \quad (1)$$

$Y_{mod}(i,j)$ is the sum of all model point source contributions plus the background value in the image pixel $[i,j]$ and N is the measured number of photons in pixel $[i,j]$. For ROSAT PSPC and HRI data the multi-component PSF (Hasinger et al., 1994b; David et al., 1996) is approximated by a single Gaussian function with a width increasing with off-axis angle. The significance ΔS of any of the individual point source contributions is then estimated by a likelihood ratio test between the best fit with and without the corresponding component. If ΔS falls below a threshold value, the corresponding component is omitted from the next iteration and only significant components are maintained. Since ΔS follows a χ^2 distribution, the errors of the best-fit parameters (68% confidence single parameter of interest) are determined by searching the parameter space for which $\Delta S = S - S_{min} = 1$. Before the next region of interest is fit, the current PSF contributions are added to the background model.

The complete source detection and parameter estimation procedure is too complicated to validate its results and e.g. quantify its detection efficiency analytically. We therefore performed extensive simulations of artificial ROSAT fields run through the same set of algorithms to study their properties (see below). Based on these simulations we have chosen a likelihood detection threshold of $\Delta S = 16$, corresponding to a 4σ detection. Formally, the probability of a spurious detection with such a threshold is 6×10^{-5} per resolution element, which would correspond to less than one spurious detection per field of view. We will see in Sect. 6 that in practice the effective detection limit is set by source confusion. Observed fluxes in the 0.5–2 keV band are calculated for each source using the detected counts, the corresponding exposure time and vignetting correction, an energy-to-flux conversion factor (ECF) and a PSF-loss correction factor (PCF) determined from simulations (see below). In order to derive the ECF we assumed a power law spectrum with photon index 2 and galactic absorption, folded through the instrument response. Table 2 gives a summary of the various energy bands and correction factors for different detectors. For the PSPC hard band, because of the restricted energy range, the ECF is almost insensitive to N_H and to the assumed spectral shape for a wide range of absorptions and

spectral indices. On the contrary, the HRI is very sensitive to absorption and spectral shape because of its lack of energy resolution. Unabsorbed sources with steep spectra are favoured by the HRI.

Table 2. Energy bands and correction factors

Detector	Band	Energy [keV]	Pulseheight Channels	ECF ^a	PCF ^b
PSPC	H	0.5-2.0	52-201	0.836	0.90
PSPC	S	0.1-0.4	11-41	1.519	0.90
PSPC	H1	0.5-0.9	52-90	0.349	0.90
PSPC	H2	0.9-2.0	91-201	0.487	0.90
HRI		0.1-2.4	1-9	0.586	0.92

^a Energy to counts conversion factor in *cts/s* for a source with 0.5–2 keV flux $10^{-11} \text{ erg cm}^{-2} \text{ s}^{-1}$

^b PSF loss correction factor from simulations

For the calculation of hardness ratios, PSPC images were also analysed in the soft (S) and the split hard (H1, H2) bands (see Table 2), however with fixed positions. The standard ROSAT soft and hard hardness ratios HR1 and HR2 have been used.

$$HR1 = \frac{H - S}{H + S} \quad HR2 = \frac{H2 - H1}{H2 + H1} \quad (2)$$

4. Astrometric corrections

The ROSAT SASS performs various corrections to the individual PSPC and HRI photons, including detector linearisation, optical distortion, boresight and attitude correction. The large set of X-ray sources with reliable optical identifications in the Lockman Hole allows for the first time to check and crosscalibrate with high accuracy the ROSAT astrometry with absolute celestial positions.

A complete sample of X-ray sources in the Lockman Hole with fluxes down to $5.5 \times 10^{-15} \text{ erg cm}^{-2} \text{ s}^{-1}$ has been optically identified (Schmidt et al., 1997, paper II). The positions of the optical counterparts have been derived from Palomar 200” CCD drift scans and have an absolute accuracy of ~ 0.5 arcsec. Using the set of point-like X-ray sources optically identified with AGN and stars, we could derive astrometrical solutions for the PSPC and HRI data, respectively. For the deep PSPC and HRI pointing observations astrometrical solutions were fit to the deviation between X-ray and optical positions. The transformations contained the following parameters: $\Delta(RA)$ and $\Delta(DEC)$ position shifts, $\Delta(\Phi)$ roll angle and $F(Sc)$ scale factor correction. The best-fit parameters were determined by a χ^2 -fit, using the individual statistical position errors of the X-ray sources and assuming an error of 0.5” for the optical positions. In order to take account

Table 3. Astrometric solutions

Instrument	Nr. IDs	E_{sys} ["]	χ^2	$F(Sc)$	$\Delta(\Phi)$ [']	$\Delta(RA)$ ["]	$\Delta(DEC)$ ["]
PSPC Pointing	47	3.0	1.28	1.0020 ± 0.0007	-2.9 ± 2.0	-0.2 ± 0.5	-0.1 ± 0.5
HRI Pointing	32	0.5	1.05	0.9972 ± 0.0006	1.2 ± 1.4	-0.1 ± 0.3	0.3 ± 0.3
HRI Raster	31	0.5	1.07	1.0004 ± 0.0006	1.0 ± 1.5	-0.3 ± 0.4	-0.3 ± 0.4
Combined	43	0.0	1.36	1.0001 ± 0.0003	-1.1 ± 0.7	-0.1 ± 0.2	0.0 ± 0.2

of possible additional deviations in the X-ray positions, which may result from residuals in the detector linearization or from X-ray source confusion, we added in quadrature a constant systematic position error E_{sys} to the statistical error for each source. The size of this additional error (see column 3 of Table 3) was chosen such that the reduced χ^2 approached a value of 1.

Table 3 shows the result of the astrometric solutions. As expected, the residual position shifts are all negligible, because all data have been shifted to a common system before. The roll angle correction applied by the SASS is already very good; the roll angle corrections $\Delta(\Phi)$ in our deep datasets are all smaller than a few arcmin. The only significant astrometrical correction which is necessary for both PSPC and HRI is a scale factor correction of order 0.2–0.3%. For the PSPC this correction factor is marginally significant and can probably be neglected for most datasets. For the HRI the scale factor error is consistent with the estimate derived from HRI data of M31 (David et al., 1996), but our data is more accurate and provide the first significant measurement of this quantity. The HRI scale factor error corresponds to a position deviation of about 4 arcsec across the HRI FOV and needs to be taken into account to achieve highest astrometrical accuracy. The residual systematic position errors across the HRI FOV are very small (0.5"), while the PSPC has residual systematic errors of order 3", most likely because of source confusion and the broader PSF (see below).

For the HRI raster scan data, every individual short pointing was first shifted to a common celestial reference system and corrected for the above scale factor error, before all photons were merged to one dataset. As a test we applied the same astrometrical transformation fit as to the pointed observations. The fact that all fit parameters are consistent with their expected values and that the required residual systematic errors are of the same order as for the individual HRI pointing shows that the shift- and merge procedure was successful. Finally, the last row in Table 3 shows an astrometric fit to the X-ray source catalogue combined from all three datasets (see below). As expected, all astrometric parameters are consistent with their expected values. The reduced χ^2 of the combined fit is acceptable without the addition of extra systematic errors. The distribution of positional errors for uniquely

identified sources is therefore as expected, thus validating the calculation of the positions and errors.

5. X-ray source catalogue

The scale factor corrections determined in the previous section were applied to the three individual detection lists from PSPC pointing, HRI pointing and HRI raster scan observation and the corresponding systematic position errors were added in quadrature to the statistical errors determined in the multi-ML detection procedure. Finally, the three individual position lists were merged into a single source list. For all detections, which were positionally coincident within their 90% error radii, weighted average positions and position errors were calculated. These form the basis for the final X-ray source catalogue, presented in Table 4. This catalogue contains all objects with PSPC fluxes higher than $1.11 \times 10^{-14} \text{ erg cm}^{-2} \text{ s}^{-1}$ at off-axis angles smaller than 18.5 arcmin and all objects with fluxes larger than $0.56 \times 10^{-14} \text{ erg cm}^{-2} \text{ s}^{-1}$ inside an off-axis angle of 12.5 arcmin.

Column (1) of Table 4 gives the official ROSAT name, column (2) an internal source number. Columns (3) and (4) give the weighted average coordinates of the X-ray sources for an equinox of J2000.0. Column (5) shows the 1σ position error of the source, including statistical and systematic errors. A capital P, H, or R after the position error indicates, whether the dominant weight to the X-ray position comes from the PSPC pointing, HRI pointing or HRI raster scan, respectively. Column 6 gives the 0.5–2 keV flux of the source in units of $10^{-14} \text{ erg cm}^{-2} \text{ s}^{-1}$, derived from the ROSAT PSPC hard band and its 1σ error. Column (7) and (8) give the soft and hard hardness ratios defined above.

6. Verification of the analysis procedure by simulations

The ROSAT deep survey exposures are probing the limits of observational and data analysis procedures. In order to obtain a reliable and quantitative characterization and calibration of the source detection procedure, detailed simulations of large numbers of artificial fields, analysed through exactly the same detection and parameter estimation procedure as the real data, are required.

Table 4. Source Catalogue

Source Name	Nr.	R.A. (2000)	Dec. (2000)	Err. [$^{\circ}$]	f_x	HR1	HR2
RX J105421.1+572545	28	10 54 21.1	57 25 44.5	1.0H	19.90 ± 0.41	1.00 ± 0.06	-0.27 ± 0.02
RX J105131.1+573440	8	10 51 31.1	57 34 40.4	0.8H	11.84 ± 0.33	-0.24 ± 0.02	-0.47 ± 0.02
RX J105316.8+573552	6	10 53 16.8	57 35 52.4	0.9H	8.82 ± 0.33	-0.29 ± 0.02	-0.40 ± 0.02
RX J105239.7+572432	32	10 52 39.7	57 24 31.7	0.8H	6.50 ± 0.30	-0.55 ± 0.02	-0.16 ± 0.03
RX J105335.1+572542	29	10 53 35.1	57 25 42.4	0.8H	5.13 ± 0.25	-0.34 ± 0.03	-0.36 ± 0.03
RX J105331.8+572454	31	10 53 31.8	57 24 53.9	0.9H	3.57 ± 0.18	-0.18 ± 0.04	-0.40 ± 0.03
RX J105339.7+573105	16	10 53 39.7	57 31 5.3	0.9H	3.56 ± 0.18	-0.59 ± 0.02	-0.43 ± 0.03
RX J105020.2+571423	56	10 50 20.2	57 14 22.8	1.8R	3.52 ± 0.17	-0.44 ± 0.02	-0.37 ± 0.04
RX J105201.5+571044	62	10 52 1.5	57 10 44.2	1.6R	3.20 ± 0.18	-0.31 ± 0.03	-0.50 ± 0.03
RX J105247.9+572116	37	10 52 47.9	57 21 16.3	0.8H	2.54 ± 0.13	-0.73 ± 0.02	-0.19 ± 0.06
RX J105410.3+573039	20	10 54 10.3	57 30 39.3	1.4H	2.43 ± 0.18	0.47 ± 0.11	-0.19 ± 0.06
RX J105154.4+573438	9	10 51 54.4	57 34 38.0	1.0H	1.88 ± 0.15	-0.23 ± 0.06	-0.18 ± 0.06
RX J105318.1+572042	41	10 53 18.1	57 20 42.0	2.4H	1.87 ± 0.13	0.03 ± 0.10	-0.46 ± 0.06
RX J105344.9+572841	25	10 53 44.9	57 28 40.5	1.1H	1.84 ± 0.15	-0.09 ± 0.07	0.13 ± 0.09
RX J105015.6+572000	42	10 50 15.6	57 20 0.2	4.7P	1.69 ± 0.15	-0.36 ± 0.06	-0.14 ± 0.07
RX J105046.1+571733	48	10 50 46.1	57 17 32.8	1.8R	1.64 ± 0.17	-0.08 ± 0.08	-0.00 ± 0.07
RX J105149.0+573249	12	10 51 49.0	57 32 48.6	1.0H	1.57 ± 0.14	1.00 ± 0.78	0.28 ± 0.08
RX J105324.6+571236	59	10 53 24.6	57 12 35.7	2.8P	1.50 ± 0.13	0.27 ± 0.14	-0.20 ± 0.07
RX J105039.7+572335	35	10 50 39.7	57 23 35.1	1.8R	1.48 ± 0.15	-0.29 ± 0.06	-0.19 ± 0.06
RX J105348.7+573033	117	10 53 48.7	57 30 33.5	1.4H	1.46 ± 0.18	1.00 ± 1.51	0.19 ± 0.10
RX J105350.3+572710	27	10 53 50.3	57 27 9.6	2.0H	1.39 ± 0.08	0.16 ± 0.17	0.18 ± 0.07
RX J105008.2+573135	73	10 50 8.2	57 31 34.7	8.2P	1.39 ± 0.13	0.78 ± 0.51	0.57 ± 0.44
RX J105243.1+571544	52	10 52 43.1	57 15 44.4	1.2H	1.32 ± 0.12	-0.36 ± 0.06	0.00 ± 0.08
RX J105108.4+573345	11	10 51 8.4	57 33 45.4	1.6H	1.27 ± 0.12	0.18 ± 0.12	0.32 ± 0.11
RX J105055.3+570652	67	10 50 55.3	57 6 51.9	8.1P	1.24 ± 0.15	0.23 ± 0.16	0.01 ± 0.11
RX J105020.3+572808	26	10 50 20.3	57 28 7.8	6.5P	1.20 ± 0.11	-0.06 ± 0.14	0.13 ± 0.11
RX J105009.3+571443	55	10 50 9.3	57 14 42.8	6.6P	1.17 ± 0.15	0.02 ± 0.06	0.13 ± 0.11
RX J105230.3+573914	2	10 52 30.3	57 39 13.8	1.3H	1.16 ± 0.14	-0.03 ± 0.17	0.01 ± 0.11
RX J105307.2+571506	54	10 53 7.2	57 15 5.6	1.9H	1.12 ± 0.14	0.05 ± 0.10	0.04 ± 0.09
RX J105319.0+571852	45	10 53 19.0	57 18 51.9	1.5H	1.04 ± 0.14	0.02 ± 0.12	-0.03 ± 0.08
RX J105137.4+573044	19	10 51 37.4	57 30 44.4	1.0H	0.99 ± 0.11	-0.24 ± 0.07	-0.18 ± 0.09
RX J105114.5+571616	504	10 51 14.5	57 16 16.0	1.8R	0.96 ± 0.12	-0.38 ± 0.07	-0.12 ± 0.09
RX J105105.2+571924	43	10 51 5.2	57 19 23.9	1.9R	0.94 ± 0.09	-0.28 ± 0.07	-0.03 ± 0.10
RX J105225.1+572304	36	10 52 25.1	57 23 3.7	1.8R	0.92 ± 0.08	0.05 ± 0.19	0.08 ± 0.11
RX J105120.2+571849	46	10 51 20.2	57 18 49.2	1.9R	0.89 ± 0.09	-0.18 ± 0.09	-0.13 ± 0.08
RX J105127.0+571129	61	10 51 27.0	57 11 29.0	6.0P	0.79 ± 0.09	-0.07 ± 0.14	-0.27 ± 0.13
RX J105329.2+572104	38	10 53 29.2	57 21 3.7	1.3H	0.78 ± 0.11	-0.30 ± 0.08	-0.53 ± 0.07
RX J105248.4+571203	60	10 52 48.4	57 12 2.7	5.0P	0.78 ± 0.10	-0.00 ± 0.19	-0.38 ± 0.09
RX J105242.5+573159	14	10 52 42.5	57 31 59.2	1.3H	0.72 ± 0.09	0.72 ± 0.52	0.44 ± 0.15
RX J105244.4+571732	47	10 52 44.4	57 17 31.9	1.6H	0.71 ± 0.09	-0.35 ± 0.08	-0.28 ± 0.10
RX J105257.1+572507	30	10 52 57.1	57 25 7.2	0.9H	0.70 ± 0.09	-0.53 ± 0.05	-0.47 ± 0.07
RX J105117.0+571554	51	10 51 17.0	57 15 54.1	5.1P	0.66 ± 0.11	0.04 ± 0.22	-0.10 ± 0.14
RX J105104.2+573054	17	10 51 4.2	57 30 53.7	1.6H	0.62 ± 0.10	0.11 ± 0.19	-0.14 ± 0.14
RX J105244.7+572122	814	10 52 44.7	57 21 22.2	1.3H	0.61 ± 0.16	0.68 ± 0.68	0.51 ± 0.18
RX J105217.0+572017	84	10 52 17.0	57 20 17.1	2.0H	0.60 ± 0.08	0.68 ± 0.71	0.85 ± 0.32
RX J105259.2+573031	77	10 52 59.2	57 30 30.8	1.1H	0.59 ± 0.10	-0.14 ± 0.13	-0.16 ± 0.14
RX J105206.0+571529	53	10 52 6.0	57 15 28.7	4.6P	0.58 ± 0.07	-0.15 ± 0.12	0.82 ± 0.17
RX J105237.7+573107	116	10 52 37.7	57 31 6.5	5.1P	0.57 ± 0.10	1.00 ± 0.84	-0.48 ± 0.09
RX J105224.7+573010	23	10 52 24.7	57 30 10.2	1.5H	0.56 ± 0.07	0.02 ± 0.20	-0.41 ± 0.10
RX J105237.9+571254	58	10 52 37.9	57 12 53.5	6.2P	0.56 ± 0.08	0.07 ± 0.21	-0.42 ± 0.09

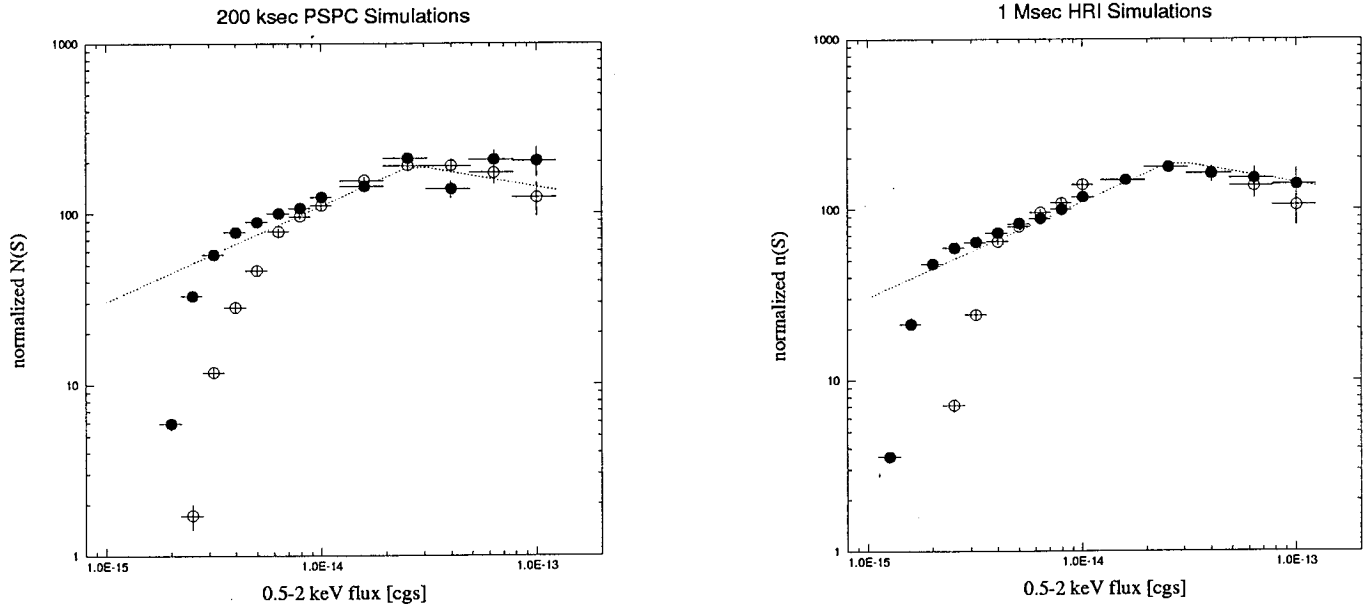


Fig. 2. Comparison of detected $\log(N)$ - $\log(S)$ relation to input source counts in the 0.5–2 keV band. The dotted line shows the differential source counts $n(S)$ input to the simulations, normalized to a Euclidean slope (see equation 3 and 4). The filled and open circles show the detected differential $\log(N)$ - $\log(S)$, derived from (a) 66 simulated PSPC fields of 200 ksec exposure, and (b) 100 simulated HRI fields of 1 Msec exposure each. Filled symbols correspond to sources at off-axis angles smaller than 12.5 arcmin for the PSPC and 10 arcmin for the HRI, respectively. Open symbols refer to larger off-axis angles.

The simulations in H93 demonstrated that source confusion sets the ultimate limit in ROSAT deep survey work with the PSPC. The crowded-field multi-ML detection algorithm used in the current paper was specifically designed to better cope with source confusion. Therefore we felt it necessary to calibrate its efficiency and verify its accuracy through new simulations. We have simulated sets of PSPC and HRI observations with 200 ksec and 1Msec exposure, respectively, approximating our current observation times. In order to compare our results with those of shallower PSPC surveys in the literature we simulated additional sets of observations of 50 and 110 ksec each. The soft X-ray $\log(N)$ - $\log(S)$ function (0.5–2 keV) has been simulated according to the ROSAT deep survey findings (H93) as a broken power law function for the differential source counts (all fluxes are given in units of $10^{-14} \text{ erg cm}^{-2} \text{ s}^{-1}$):

$$\begin{aligned} n(S) &= n_1 \times S^{-b_1} \text{ for } S > S_b, \quad n_1 = 238.1 \quad b_1 = 2.72 \\ &= n_2 \times S^{-b_2} \text{ for } S < S_b, \quad n_2 = 111.0 \quad b_2 = 1.94 \quad (3) \\ S_b &= 2.66 \end{aligned}$$

As shown in H93, the final results are relatively independent from the actual $\log(N)$ - $\log(S)$ parameters chosen for the artificial fields. In the simulations point sources are placed at random within the FOV, with fluxes drawn at random from the $\log(N)$ - $\log(S)$ function down to a minimum source flux of 4.65×10^{-18} , where formally all the X-ray background is resolved for the assumed source counts.

(For the later comparison between input and output catalogues only input sources with fluxes larger than 10^{-16} or more than 5 simulated photons are maintained in the input catalogue.) For each source the ROSAT vignetting correction, the corresponding ECF (see Table 2) and the exposure time (50, 110, 200 ksec for PSPC, 1Msec for HRI) are applied to the source flux to obtain the expected number of source counts. The actual source counts are drawn from a Poissonian distribution and folded through the point spread function. The realistic multi-component point spread function model is taken from Hasinger et al. (1994b) for the PSPC and from David et al. (1996) for the HRI. Finally, all events missing in the field, i.e. particle background, non-source diffuse background and photons not simulated in the $\log(N)$ - $\log(S)$ function are added as a smooth distribution to the image.

A total of 66 PSPC fields of an exposure of 200 ksec, 50 fields of 50 ksec and 27 fields of 110 ksec each has been simulated in the 0.5–2 keV band. The corresponding number of HRI fields with 1 Msec exposure was 100. All simulated exposures have been analysed through exactly the same sequence of detection, background estimation and parameter estimation algorithms as the real data. The 200 ksec PSPC images were analysed in two ranges of off-axis angles: 0–12.5 arcmin and 12.5–18.5 arcmin, the HRI 1Msec images for off-axis angle ranges of 0–10 arcmin and 10–15 arcmin and the 50 and 110 ksec PSPC exposures inside 15 arcmin.

6.1. Flux conservation

For each detected source the process of “source identification” has been approximated by a simple positional coincidence check. A detected source was identified with the counterpart from the input list, which appeared closest to the X-ray position within a radius of 30 arcsec. A direct comparison between the detected and simulated number of photons for sources with fluxes brighter than 5×10^{-14} cgs shows, that the scale of the output flux is the same as that of the input flux to an accuracy of better than 1%. This means that at bright fluxes no systematic errors exist, apart from the PSF loss factor of 0.90 (see Table 2), which is corrected for globally in the simulations as well as in the real data. This correction is necessary, probably due to the misfit between the broader components of the real PSF and the simple Gaussian model in the multi-ML fit. For the HRI this PSF loss factor is 0.92 (see Table 2).

6.2. Limiting sensitivity and $\log(N)$ - $\log(S)$ relation

A $\log(N)$ - $\log(S)$ function has been derived for the simulated detected sources (in rings of 0–12.5 arcmin and 12.5–18.5 arcmin for the PSPC and rings of 0–10 arcmin and 10–15 arcmin, respectively for the HRI). For easier comparison the differential source counts $n(S)$ were divided by the source counts expected for a Euclidean distribution, i.e.:

$$n(S)_{cor} = n(S) \times S^{2.5} \quad (4)$$

Fig. 2 shows the comparison between the input $\log(N)$ - $\log(S)$ and the detected number counts in this representation for both 200 ksec PSPC and the 1 Msec HRI simulations. The faintest sources detected in the PSPC at small off-axis angles have a flux of 2×10^{-15} cgs. For a flux lower than 3×10^{-15} cgs, the source counts fall significantly below the simulated $\log(N)$ - $\log(S)$ function, while above this flux there is a slight excess. These effects are well known from ROSAT PSPC deep survey simulations and are due to a number of selection and confusion effects. At larger off-axis angles the sensitivity is reduced correspondingly. The faintest HRI sources reach down to fluxes of 10^{-15} cgs and the deviation between input and output source counts becomes insignificant above a flux of 1.8×10^{-15} cgs for small off-axis angles. Again, at larger angles the sensitivity is reduced. The source confusion effects are much less pronounced in the HRI.

The deviation between input- and output source counts in the simulations can be used to correct the observed $\log(N)$ - $\log(S)$ function down to the faintest limiting fluxes (see H93). Utilizing all sources detected in the real PSPC and HRI pointing observations inside off-axis angles of 18.5 and 15 arcmin, respectively, we calculated the corrected observed $\log(N)$ - $\log(S)$ function displayed in Fig. 3. The new PSPC data agree very well with the source

counts published earlier and extend those down to a flux of 2×10^{-15} cgs and a surface density of $640 \pm 75 \text{ deg}^{-2}$. The HRI $\log(N)$ - $\log(S)$ function for the first time extends the source counts down to fluxes of 10^{-15} cgs and reaches a surface density of $970 \pm 150 \text{ deg}^{-2}$, about a factor of two higher than any previous X-ray determination of source counts. All data are consistent with the previous determination of source counts and fluctuation limits (H93).

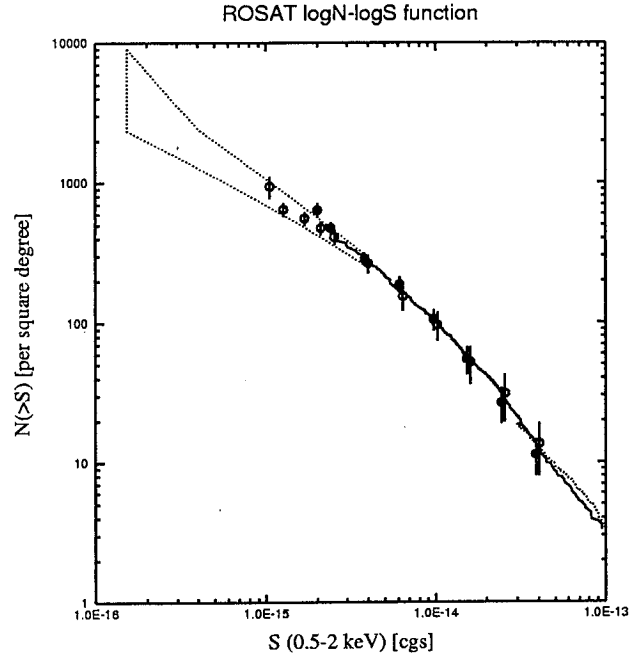


Fig. 3. Measured ROSAT $\log(N)$ - $\log(S)$ function in the Lockman Hole. Filled circles give the source counts from the 207 ksec PSPC observation. Open circles are from the ultradeep HRI observation (1112 ksec), slightly shifted in flux in order to avoid overlap of error bars. The data are plotted on top of the source counts (solid line) and fluctuation limits (dotted area) from Hasinger et al. (1993). The dotted line at bright fluxes refers to the total source counts in the RIXOS survey (Mason et al., 1996, priv. comm.).

6.3. Source confusion

The detected source catalogues are affected by biases and selection effects present in the source-detection procedure. The most famous of those is the Eddington bias, which produces a net gain of the number of sources detected above a given flux limit as a consequence of statistical errors in the measured flux (see discussion in H93). Another selection effect, most important in the deep fields considered here, is source confusion. The net effect of source confusion is difficult to quantify analytically, because it can affect the derived source catalogue in different ways:

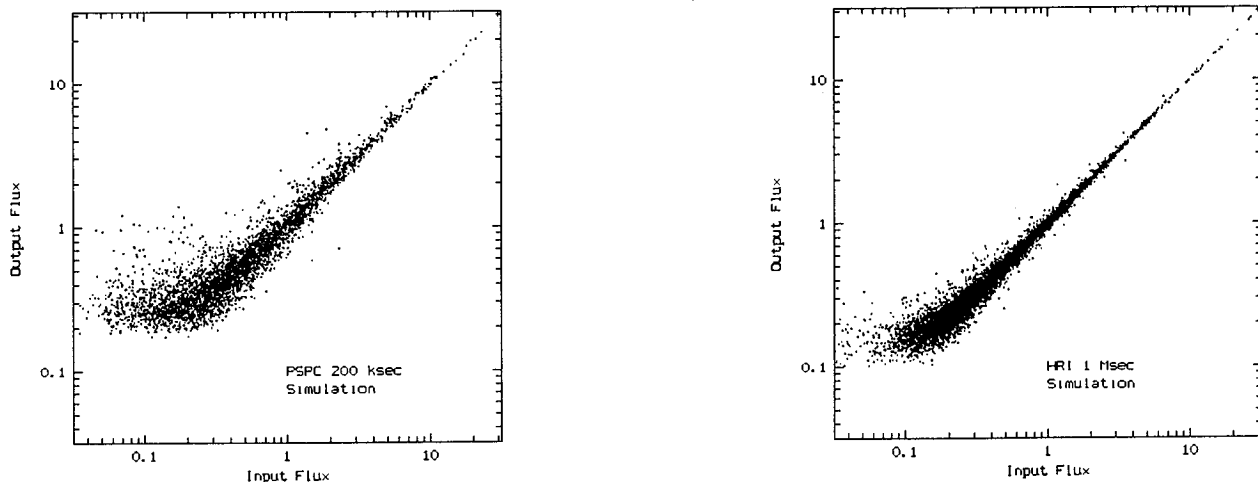


Fig. 4. Detected flux versus input flux for (a) 66 simulated PSPC fields of 200 ksec exposure, and (b) 100 simulated HRI fields of 1 Msec exposure each. The PSPC data is for off-axis angles smaller than 12.5 arcmin, for the HRI the limit is 10 arcmin. Fluxes are in units of $10^{-14} \text{ erg cm}^{-2} \text{ s}^{-1}$.

(1) two sub-threshold sources could be present in the same resolution element and thus mimic a single detected source. This leads to a net gain in the number of sources, similar to the Eddington bias.

(2) two sources above the threshold could merge into a single brighter source. In this case one source is lost and one is detected at a higher flux. Whether the total flux is conserved or not depends on the distance between the two sources and on the details of the source detection algorithm.

(3) the detection algorithm cannot discriminate close sources with very different brightness, which results in a net loss of fainter sources.

The effects of confusion become immediately obvious in fig 4 where for each detected source the detected flux is compared to the flux of the nearest input source within $30''$. While for bright sources there is an almost perfect match, there is a significant systematic deviation for fainter X-ray sources, where most objects appear at fluxes significantly brighter than their input counterparts, which is a direct indication of confusion because every detected source is only associated with one input source while its flux may be contributed from several sources.

We can quantify “confusion” e.g. by looking for sources, whose detected X-ray flux is significantly larger than their input flux. This means that a substantial fraction of the detected photons originates from other, contaminating sources. We define SR as the ratio of the de-

tected flux and the input flux increased by 3 times the statistical error:

$$SR = \frac{S_{det}}{S_{inp}} \cdot \frac{1}{1 + 3\sigma_S} \quad (5)$$

where σ_S is the fractional flux error. For practical purposes a flux ratio of $SR > 1.5$ has been chosen, above which significant position deviations might be expected. In Table 5, we give the *fraction of contaminated sources* FC with flux ratio SR larger than 1.5 as a function of detected flux for different surveys. Significant confusion (larger than 10%) sets in below a flux of $5 \times 10^{-15} \text{ cgs}$ for the 200 ksec PSPC observation and below 10^{-14} cgs for the 50 ksec observation. In contrast, the HRI confusion is negligible over almost the complete range of detected fluxes.

6.4. Effect of source confusion on optical identification

While it is obviously possible to correct for confusion effects on the source counts in a statistical way, the optical identification process relies on the position of individual sources. An independent measure of confusion is the fraction of sources with significant positional deviation from their respective counterparts. Fig. 5 shows for each simulated source the distance to the nearest output source as a function of simulated input flux. As expected, bright sources have relatively small positional errors and therefore small deviations of a few arcsec between simulated and output position. For fainter sources there is an incompleteness limit. More and more input sources are not

Table 5. Confusion estimates^a

Flux range ^b [10^{-14} cgs]	200 ksec PSPC 0–12.5'			200 ksec PSPC 12.5–18.5'			110ksec PSPC 0–15'			50 ksec PSPC 0–15'			1 Msec HRI 0–10'		
	FC	FL	FU	FC	FL	FU	FC	FL	FU	FC	FL	FU	FC	FL	FU
2-10	2	1	0	6	3	8	3	2	2	1	1	1	0	0	0
1-2	3	4	3	9	14	11	7	3	5	4	7	7	0	0	0
0.5-1	7	10	5	14	38	26	9	19	11	11	33	19	1	0	0
0.2-0.5	12	38	16	16	78	34	11	62	22	14	74	19	2	3	1
0.1-0.2	20	81	24										11	47	10

^a Fraction of confused sources in percent according to different confusion measures (see text): FC is the percentage of contaminated sources, having an output flux significantly larger than their input flux ($SR > 1.5$). FL is the percentage of lost sources, having no detected source within $15''$ from the input position. FU is the fraction of unidentifiable detected sources, having no input source within $15''$ from the detected position. ^b detected flux for FC and FU, input flux for FL

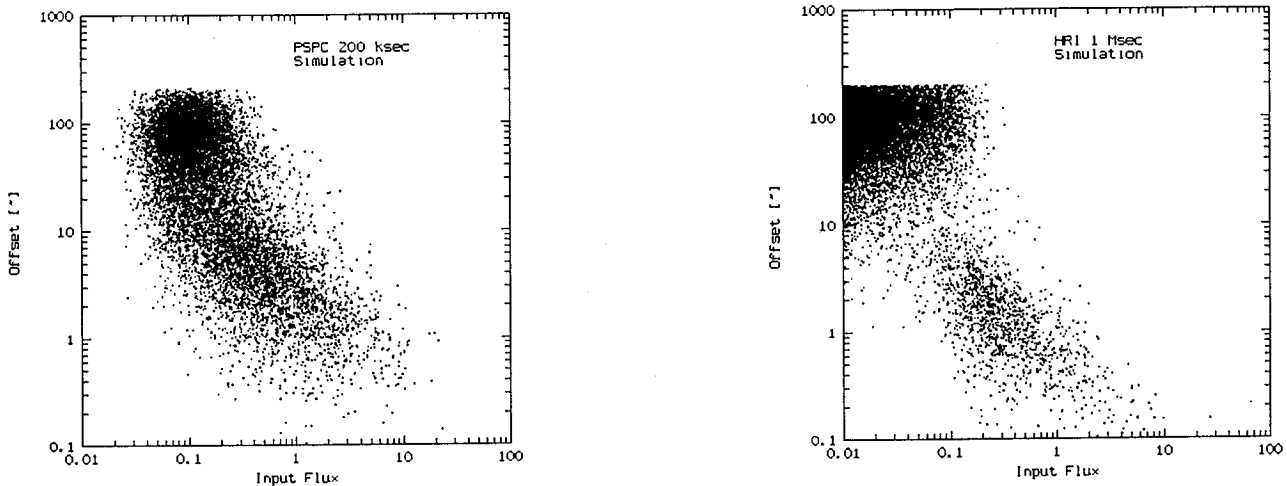


Fig. 5. Position deviation between input source and nearest output object as a function of input flux for the simulations in Fig. 2. The plot is cut off artificially for distances larger than 200 arcsec.

detected at all and therefore are matched to the nearest (but wrong) detected X-ray source. For the HRI simulation this yields a well-defined cloud of spuriously matched sources below a flux of $\sim 2 \times 10^{-15}$ cgs. For the PSPC this incompleteness limit sets in below $\sim 4 \times 10^{-15}$ cgs and the spurious match cloud is not disjunct of the detected source correlation track. Confusion leads to a halo of PSPC sources with significantly larger positional deviation than the bulk of detected sources at the same flux. A practical limiting radius for the optical identification of faint ROSAT X-ray sources is $15''$, which is used by several authors (see e.g. Bower et al., 1996, Georgantopoulos et al., 1996). In Table 5 we give the *fraction of lost sources* $FL(> 15'')$ which have no detected source within a distance of $15''$ from the input position.

The quantity FL is a good tool to define a reliable flux limit for a survey, because it combines both the confusion

and incompleteness effects. For practical applications we need, however, a quantity that can be applied to existing surveys, i.e. to detected sources. To do this, we invert the question that led to the quantity FL and ask: how many of the detected sources appear at a detected position further away from any "reasonable" input position than e.g. $15''$. For this purpose we exclude as reasonable input positions sources with input fluxes more than a factor 3 below the detected flux. This gives us an estimate of the *fraction of unidentifiable sources* in a survey, which we denote with the quantity FU.

The quantities FC, FL and FU are compared in Table 5 for different surveys and flux ranges. This table shows that, as expected, confusion effects increase dramatically towards fainter fluxes. For fluxes above the incompleteness limit the different confusion measures, FC, FL and FU lead to similar estimates for the number of confused

sources. Below this limit, FL increases dramatically, indicating severe incompleteness of the survey in addition to confusion. Using this table we have chosen the relatively conservative limits in flux and off-axis angles employed in the current survey, i.e. a flux limit of 5.5×10^{-15} for off-axis angles smaller than 12.5 arcmin and a flux limit of 1.1×10^{-14} for off-axis angles between 12.5 and 18.5 arcmin. In the discussion section we compare these simulations to shallower PSPC surveys in the literature.

7. Discussion

With a limiting flux of $\sim 10^{-15} \text{ erg cm}^{-2} \text{ s}^{-1}$, the X-ray survey in the *Lockman Hole* represents the deepest X-ray survey ever performed. The total observing time invested is quite comparable to that of other major astronomical projects, like e.g. the Hubble Deep Field (Williams et al., 1996). Because of the expected confusion in the PSPC it was clear from the beginning, that HRI data would be necessary to augment the PSPC identification process. Because of the smaller field-of-view of the HRI and because of its lower quantum efficiency, it was necessary to invest about a factor five more HRI time than PSPC time. Both the HRI raster scan, which provides excellent positions for all brighter objects in the PSPC field, and the HRI ultradeep survey in the (slightly offset) central part of the field allow almost complete optical identifications of sources down to $5.5 \times 10^{-15} \text{ erg cm}^{-2} \text{ s}^{-1}$ (see paper II). Apart from this, the ultradeep HRI data provides a survey in its own right, which is not yet fully exploited. It will ultimately lead to reliable optical identifications a factor of 3-4 deeper than the current survey. On the other hand, the *Lockman Hole* data are also of fundamental importance for other observations with the ROSAT HRI since they provided for the first time a significant determination of the HRI scale factor correction which is important for all high-quality astrometry with the HRI.

7.1. The ROSAT $\log(N)$ - $\log(S)$ function

The new PSPC and HRI data shown in Fig. 3 carry the resolved source counts a factor of 2.5 deeper than the most sensitive previous determinations (H93, Branduardi-Raymont et al., 1994). It is very reassuring to see that the source counts are still consistent with the previous fluctuation analyses (H93, Barcons et al., 1994). There are, however, some problems at the bright end of the source counts. In our previous paper we used the source counts from the EMSS (Gioia et al., 1990) to constrain the bright end ($S_{(0.5-2.0\text{keV})} > 1.8 \times 10^{-13}$) of the $\log(N)$ - $\log(S)$ relation. The first study to note a discrepancy between the EMSS and ROSAT counts was the RIXOS survey. Page et al. (1996) found, that the EMSS $\log(N)$ - $\log(S)$ for AGN is significantly lower than the one from RIXOS. The source counts from the ROSAT All-Sky-Survey Bright Source Catalogue (Voges et al., 1996) confirm this trend and ex-

tend it to fluxes well above $10^{-12} \text{ erg cm}^{-2} \text{ s}^{-1}$ (Hasinger et al., 1997, in prep.). It appears that the $\log(N)$ - $\log(S)$ function at fluxes brighter than $10^{-13} \text{ erg cm}^{-2} \text{ s}^{-1}$ has a slope of $\beta_0 \sim 2.3$ and a normalization of ~ 91 and is therefore significantly flatter than what we assumed in H93 from a fit to the EMSS total source counts. The flatter $\log(N)$ - $\log(S)$ slope at bright fluxes has some consequences for the calculation of the resolved fraction.

7.2. The resolved fraction

As in H93 we restrict the analysis of the resolved fraction to the energy band 1-2 keV in order to minimize galactic contamination in the X-ray background spectrum. The absolute level and the spectrum of the X-ray background in this energy range is still a matter of debate (see the discussion in Hasinger 1996). In H93 we assumed a 1-2 keV background flux of $1.25 \times 10^{-8} \text{ erg cm}^{-2} \text{ s}^{-1} \text{ sr}^{-1}$. From ASCA data in the energy range 1-7 keV, Gendreau et al. (1995) have derived a flat spectrum with photon index 1.4 and a normalization of $8.9 \text{ keV cm}^{-2} \text{ s}^{-1} \text{ keV}^{-1}$ at 1 keV. Integrating this spectrum we derive a lower limit to the 1-2 keV XRB flux of $1.22 \times 10^{-8} \text{ erg cm}^{-2} \text{ s}^{-1} \text{ sr}^{-1}$. This can be contrasted to the earlier ROSAT PSPC determination of a steep spectrum in the 0.5-2 keV band, with photon index around 2 and a normalization around 13 (see Hasinger 1996). Integrating this over the 1-2 keV band yields a flux of $1.44 \times 10^{-8} \text{ erg cm}^{-2} \text{ s}^{-1} \text{ sr}^{-1}$, which is consistent with the background flux derived by Chen et al., 1997 from a joint ROSAT/ASCA fit (1.46 in the same units).

In H93 we integrated the analytic $\log(N)$ - $\log(S)$ function (Eq. 3) for fluxes brighter than $2.5 \times 10^{-15} \text{ erg cm}^{-2} \text{ s}^{-1}$, including a fit to the EMSS at fluxes brighter than $1.8 \times 10^{-13} \text{ erg cm}^{-2} \text{ s}^{-1}$. We obtained a resolved 1-2 keV flux of $0.74 \times 10^{-8} \text{ erg cm}^{-2} \text{ s}^{-1} \text{ sr}^{-1}$. If we follow the same prescription, but now integrating the H93 source counts above our limiting flux of $10^{-15} \text{ erg cm}^{-2} \text{ s}^{-1}$, we arrive at a resolved flux of 0.89 in the same units. If we, however, correct for the flatter slope of the bright end $\log(N)$ - $\log(S)$ (see above), we arrive at a resolved flux value of 0.99 (same units). We use this resolved flux in comparing with the total diffuse background in the 1-2 keV band.

If we adopt a 1-2 keV background flux of $1.45 \times 10^{-8} \text{ erg cm}^{-2} \text{ s}^{-1} \text{ sr}^{-1}$, we have resolved 68% of the 1-2 keV X-ray background at a flux of $10^{-15} \text{ erg cm}^{-2} \text{ s}^{-1}$. If, however, the lower ASCA spectrum with a flux of $1.22 \times 10^{-8} \text{ erg cm}^{-2} \text{ s}^{-1} \text{ sr}^{-1}$ holds, we have already resolved 81% of the background. We see, that the uncertainty in the resolved fraction is now dominated by the systematic error in the absolute background flux and not by the source counts. As a best guess for the resolved fraction we take 70 - 80%.

Table 6. Comparison of ROSAT surveys

Survey ^a	Area ^b	T ^c	S _{lim} ^d	Off ^e	Err ^f	S _{range} ^g	FC ^h	FL ⁱ	FU ^j
RIXOS	~ 20	>8	3.0						
CRSS	3.9	>6	2.0						
DRS	1.4	21-49	0.3	15	15	0.3-0.6	13	62	23
MARA	0.2	55	0.5	15	15	0.5-1	11	33	19
NEP	0.2	79	1.0	15.5	15	1-2	6	6	7
UKDS	0.2	110	0.2	15	10	0.2-0.4	10	76	42
RDS	0.3	207	0.5	12.5	15	0.5-1	7	10	5
HRI	0.1	1000	0.2	12.5	5	0.2-0.4	2	7	5

^a cf. text for explanation of acronyms

^b approximate, in square degrees

^c PSPC exposure time, in ksec

^d quoted limiting flux $S(0.5 - 2\text{keV})$ in units of $10^{-14} \text{ erg cm}^{-2} \text{ s}^{-1}$

^e maximum off-axis angle in survey in arcmin

^f radius of error circle searched in survey in arcsec

^g flux range for which FC, FL and FU have been estimated

^h percentage FC of contaminated objects

ⁱ percentage FL of lost objects

^j percentage FU of unidentifiable objects

7.3. Comparison to shallower PSPC surveys

The optical identifications in the *Lockman Hole* and the detailed comparison with other work is described in paper II (Schmidt et al., 1997). Here we want to draw global comparisons with other PSPC surveys, in particular applying the simulation results described above. Quite a number of groups are involved in optical identifications of deep and medium-deep survey fields observed with ROSAT (see Table 6) and already many papers have been written about the interpretation of ROSAT survey results. Among the most debated findings is the claimed detection of a possible new class of X-ray active, optically relatively normal emission line galaxies at faint flux levels (Griffiths et al., 1996, McHardy et al., 1997). Unfortunately, however, only very few surveys so far have been published formally (i.e. including a catalogue of detected sources and a detailed description of the detection and identification procedure), so that quantitative comparisons can be made. Among those published are the Cambridge-Cambridge ROSAT Serendipity Survey (CRSS, Boyle et al., 1995), a small part of the deep ROSAT survey (DRS, Shanks et al., 1991, see also Georgantopoulos et al., 1996) and the North Ecliptic Pole Survey (NEP, Bower et al., 1996). Among those waiting to be fully published are the ROSAT International X-ray Optical Survey (RIXOS, Mason et al., in prep., see also Page et al., 1996), the UK ROSAT deep field survey (UKDS, McHardy et al., 1997), the full DRS, the survey in the Marano field (MARA, Zamorani et al., in prep.), and finally our own ROSAT Deep Survey (RDS, this paper; Schmidt et al., 1997). Nevertheless, the global properties of these surveys are known and some details can be ob-

tained from the existing literature. See Table 6 for a summary of the surveys in question. The table also includes a prediction for the HRI ultradeep survey.

Using the experience gained from the ROSAT Deep Survey and applying the simulation tools to the shallower surveys we can now make some statements about the expected quality of the other surveys, in particular with respect to possible confusion and the corresponding optical misidentification. As we have seen in Table 5, various confusion problems, as indicated by the FL, FC and FU percentages, become severe roughly within a factor of 2 from the formal detection threshold of a PSPC exposure longer than 50 ksec. It is interesting to note that this behaviour is not a strong function of the exposure time. In order to obtain a more quantitative assessment of the different surveys, we use our PSPC simulations of 50 ksec (DRS, MARA), 110 ksec (UKDS) and 200 ksec (RDS) exposures applying as far as possible the detailed information about exposure times, quoted flux limit, off-axis angles and assumed error circle radii in the individual surveys (see Table 6). For the 80 ksec NEP survey we use quantities interpolated between the 50 ksec and the 110 ksec simulations. For lack of even shallower simulations we do not make statements about the RIXOS and CRSS surveys. For each of the deep and medium-deep surveys in Table 6 we calculate the quantities FC, FL and FU, for a flux range within a factor of two from the sensitivity limit quoted by the authors. This way we can predict for each survey the fraction of misidentified sources among the faint source population, where presumably the new discoveries would be expected.

It is not surprising to see, that those surveys that employ a relatively conservative limiting sensitivity (as judged from the ratio between exposure time and flux limit) have very small fractions of unidentifiable sources. This is confirmed by the high rate of identifications e.g. for the NEP survey (Bower et al., 1996) and the RDS (Schmidt et al., 1997). The RDS is additionally helped by the HRI data in the field. Larger fractions of unidentifiable sources on the order of 10% are expected for the DRS and the Marano survey. Indeed, in the Marano field, which unfortunately does not have HRI coverage, we see a significant number of empty error boxes (Zamorani et al., in preparation). Unidentified source fractions of order 20% are no major problem as long as one is studying majority populations of X-ray sources (e.g. AGN). They are, however, already a substantial problem if one tries to identify new classes of objects which necessarily are minority classes. There the error can easily approach 100%. For the UKDS, which tried to push deepest in the optical identification, unfortunately the largest unidentifiable fraction (42%) is expected. Indeed, about 26% out of a total of 34 UKDS sources fainter than $5 \times 10^{-15} \text{ erg cm}^{-2} \text{ s}^{-1}$ are unidentified (as derived from Fig. 5 in McHardy et al., 1997), either because the error boxes are empty or contain too faint objects. Judging from our simulations we also expect some of the UKDS sources with proposed optical counterparts to be misidentified.

8. Conclusions

We have presented the complete catalogue of 50 X-ray sources with 0.5–2 keV fluxes above $5.5 \times 10^{-15} \text{ erg cm}^{-2} \text{ s}^{-1}$ from the ROSAT Deep Survey pointing of exposure time 207 ksec in the Lockman Hole. The X-ray positions are largely defined by additional ROSAT HRI observations of more than 1Msec total exposure time. Using the HRI data we have derived a new $\log(N)$ - $\log(S)$ function reaching a source density of $970 \pm 150 \text{ deg}^{-2}$ at a limiting flux of about $10^{-15} \text{ erg cm}^{-2} \text{ s}^{-1}$. At this level 70–80% of the 0.5–2 keV X-ray background is resolved into discrete sources. The observations and the analysis procedure specifically developed to cope with confused X-ray observations have greatly profited from detailed simulations of PSPC and HRI fields. Based on these simulations we have defined conservative limits on flux and on off-axis angles, which guarantee a high reliability of the catalogue. The fraction of confused or unidentifiable sources in the catalogue is expected at only a few percent, but is probably even lower due to the existence of the deep HRI data.

We also discussed simulations of shallower fields and show that surveys, which are only based on PSPC exposures larger than 50 ksec, become severely confusion limited typically a factor of 2 above their 4σ detection threshold. Sizeable fractions of confused and unidentifiable sources are expected for some of the published surveys. This may have consequences for some recent claims of a

possible new source population emerging at the faintest X-ray fluxes.

Acknowledgements. The ROSAT project is supported by the Bundesministerium für Forschung und Technologie (BMFT), by the National Aeronautics and Space Administration (NASA), and the Science and Engineering Research Council (SERC). This work was supported in part by NASA grants NAG5-1531 (M.S.), NAG8-794, NAG5-1649, and NAGW-2508 (R.B. and R.G.). G.H. acknowledges the grant FKZ 50 OR 9403 5 by the Deutsche Agentur für Raumfahrtangelegenheiten (DARA). G.Z. acknowledges partial support by the Italian Space Agency (ASI) under contract ASI 95-RS-152.

References

- Barcons X., Branduardi-Raymont G., Warwick R.S., et al., 1994, MNRAS 268, 833
- Bower R. G., Hasinger G., Castander F. J., et al., 1996, MNRAS, 281, 59
- Boyle B.J., Griffiths R.E., Shanks T., et al. 1993, MNRAS 260, 49
- Boyle B.J., Shanks T., Georgantopoulos I., et al., 1994, MNRAS 271, 639
- Boyle B.J., McMahon R.G., Wilkes B.J., Elvis M., 1995, MNRAS 272, 462
- Branduardi-Raymont G., Mason K.O., Warwick R.S. et al., 1994, MNRAS 270, 947
- Cagnoni I., Della Ceca R., Maccacaro T., 1997, ApJ (submitted)
- Cash W., 1979, ApJ 228, 939
- Chen L.-W., Fabian A.C., Gendreau K.C., 1997, MNRAS 285, 449
- Comastri A., Setti G., Zamorani G., Hasinger G., 1995, A&A 296, 1
- David F.R., Harnden Jr. F.R., Kearns K.E., et al., 1996, in: The ROSAT Users Handbook, Briel et al., eds.
- Gendreau K.C., Mushotzky R., Fabian A.C., et al., 1995, PASJ 47, L5
- Georgantopoulos I., Stewart G.C., Shanks T., et al., 1996, MNRAS, 280, 276
- Giacconi R., Gursky H., Paolini F. R., Rossi B. B., 1962, Phys. Rev. Lett., 9, 439
- Giacconi R., Bechtold J., Branduardi G., et al. 1979, ApJ 234, L1
- Gioia I., Maccacaro T., Schild R.E., et al. 1979, ApJS 72, 567
- Griffiths R.E., Murray S.S., Giacconi R., et al. 1983, ApJ 269, 375
- Griffiths R.E., Della Ceca R., Georgantopoulos I., et al., 1996, MNRAS, 281, 71
- Hamilton T.T., Helfand D.J., Wu X., 1991, ApJ 379, 576
- Hasinger G., 1996, IAU Symp. 168, 245
- Hasinger G., Burg R., Giacconi R. et al., 1993, A&A 275, 1 (erratum A&A 291, 348) (H93)
- Hasinger G., Johnston H., Verbunt F., 1994a, A&A 288, 466
- Hasinger G., Boese G., Predehl P., et al., 1994b, Legacy 4, 40, MPE/OGIP Calibration Memo CAL/ROS/93-015
- Inoue H., Kii T., Ogasaka Y., et al., 1996, in *Röntgenstrahlung from the Universe*, H.-U. Zimmermann, J. Trümper, H. Yorke, eds., MPE report 263, p. 323

- Jones L.R., McHardy I.M., Merrifield M.R. et al., 1996 MN-RAS submitted (astro-ph/9610124)
- Lockman F.J., Jahoda K., McCammon D., 1986, ApJ 302, 432
- McHardy I.M., Jones L.R., Merrifield M.R. et al., 1997 MN-RAS submitted (astro-ph/9703163)
- Page M.J., Carrera F.C., Barcons X. et al., 1996, MNRAS 281, 579
- Pfeffermann E., Briel U.G., 1992, IEEE Trans. Nucl. Sci., vol. 39, no. 4, p.976
- deRuiter H.R., Zamorani G., Parma P. et al., 1997, A+A 319, 7
- Schmidt M., Hasinger G., Gunn J., et al., 1997, A&A, in press (Paper II)
- Shanks T., Georgantopoulos I., Stewart G.C., et al. 1991, Nature 253, 315
- Voges W., 1992 in: Proc. ESA ISY Conference, ESA ISY-3, p.9
- Voges W., Aschenbach B., Boller T., et al., 1996, IAU Circ. 6420
- Williams R.E., Blacker B., Dickinson M., et al., 1996, AJ 112, 1335
- Zdziarski A.A., 1996, MNRAS 281, L9
- Zimmermann H.U., Becker W., Belloni T., et al., 1994, MPE report 257

A&A manuscript no. 1998
(will be inserted by hand later) A & A 329, 495
Your thesaurus codes are:
03(04.19.1;11.01.2;11.17.2;11.19.1;13.25.2)

NAGW-2508

ASTRONOMY
AND
ASTROPHYSICS
14.5.1998

The ROSAT Deep Survey

II. Optical identification, photometry and spectra of X-ray sources in the Lockman field

M. Schmidt¹, G. Hasinger², J. Gunn³, D. Schneider⁴, R. Burg⁵, R. Giacconi⁶, I. Lehmann², J. MacKenty⁷, J. Trümper⁸, and G. Zamorani^{9,10}

¹ California Institute of Technology, Pasadena, CA 91125, USA

² Astrophysikalisches Institut Potsdam, An der Sternwarte 16, 14482 Potsdam, Germany

³ Princeton University Observatory, Princeton, NJ 08540, USA

⁴ Pennsylvania State University, University Park, PA 16802, USA

⁵ Johns Hopkins University, Baltimore, MD 21218, USA

⁶ European Southern Observatory, Karl-Schwarzschild-Str. 1, 85748 Garching bei München, Germany

⁷ Space Telescope Science Institute, 3700 San Martin Drive, Baltimore, MD 21218, USA

⁸ Max-Planck-Institut für extraterrestrische Physik, Karl-Schwarzschild-Str. 2, 85740 Garching bei München, Germany

⁹ Osservatorio Astronomico, Via Zamboni 33, 40126 Bologna, Italy

¹⁰ Istituto di Radioastronomia del CNR, via Gobetti 101, I-40129, Bologna, Italy

Received 12 May 1997; accepted 11 Sep 1997

Abstract. The ROSAT Deep Survey includes a complete sample of 50 X-ray sources with fluxes in the 0.5 – 2 keV band larger than $5.5 \cdot 10^{-15}$ erg cm⁻² s⁻¹ in the *Lockman* field (Hasinger et al., Paper I). We have obtained deep broad-band CCD images of the field and spectra of many optical objects near the positions of the X-ray sources. We define systematically the process leading to the optical identifications of the X-ray sources. For this purpose, we introduce five identification (ID) classes that characterize the process in each case. Among the 50 X-ray sources, we identify 39 AGNs, 3 groups of galaxies, 1 galaxy and 3 galactic stars. Four X-ray sources remain unidentified so far; two of these objects may have an unusually large ratio of X-ray to optical flux.

Key words: surveys – galaxies: active – quasars: emission lines – galaxies: Seyfert – X-rays: galaxies

1. Introduction

The goal of the ROSAT Deep Survey (RDS) is to obtain information about the luminosity functions of various types of X-ray sources as well as their evolution with redshift, and to understand the origin of the X-ray background (XRB) discovered more than thirty years ago (Gi-

aconi et al. 1962). The survey was conducted in the *Lockman* field (Hasinger et al. 1993), which has a minimum of galactic hydrogen column density (Lockman et al. 1986). The survey consists of exposures totaling 207 ksec with the ROSAT PSPC and a raster scan of HRI exposures totaling 205 ksec. In addition, we have a series of HRI exposures of a fixed area within the PSPC field with a total exposure of 1112 ksec, which allows us to derive improved positions for PSPC sources detected in the area.

The extraction of the X-ray sources and the derivation of the limiting X-ray flux of detection and other X-ray properties are presented in Paper I (Hasinger et al. 1997). Radio observations of the *Lockman* field have been published by De Ruiter et al. (1997).

This paper presents the optical observations made in the *Lockman* field. These consist of CCD imaging of the field and spectroscopic observations of optical objects close to the position of the X-ray sources. Section 2 covers the CCD imaging, the extraction of the optical objects, their positions and magnitudes. In Sect. 3, we discuss the spectroscopic observations of optical candidates for identification with the X-ray sources. On the basis of these observations and the X-ray properties, we obtain optical identifications and classifications for almost all of the X-ray sources, cf. Sect. 4. In Sect. 5, we compare our results to those of other surveys made with ROSAT and in Sect. 6 we summarize the results. Throughout the paper, we use $H_0 = 50$ km s⁻¹ Mpc⁻¹ and $q_0 = 0.5$.

Send offprint requests to: G. Hasinger

15 Sep 1997
astro-ph/9709144

2. Optical imaging and photometry of the Lockman field

As described below, we carried out imaging observations of the field at Mauna Kea and at Palomar. Efforts to observe the field at Kitt Peak National Observatory were unsuccessful due to weather.

2.1. CCD imaging at the University of Hawaii 2.2-m telescope

Images of the *Lockman* field were obtained on 16-19 January, 1988 with the University of Hawaii 2.2-m telescope. The detector was an 800x800 thinned Texas Instruments CCD obtained from the NSF distribution. A focal reducer in the cassegrain camera produced an image scale of $0''.355$ per pixel; the field of view was $4'.73$ on a side. A mosaic of 50 frames was taken through B and R filters on the Kron-Cousins system to cover most of the area in the inner $20'$ of the PSPC field. Exposure times were 10 min. for the B filter, and 4 min. for R. Photometric calibration was provided each night by several observations of the M67 asterism (Chevalier & Ilovaisky 1991). Typical seeing for the nights ranged between $1''.0$ and $1''.5$. The FOCAS image processing system (Valdes 1982) was used for processing the images and to produce total magnitudes and morphological classes. The magnitude limits were around 24.5 in B and 23.5 in R.

2.2. CCD drift scans at the Palomar 5-m telescope

Drift scans of the *Lockman* field through two filters were obtained on March 29, 1989 with the 4-Shooter camera (Gunn et al. 1987) at the cassegrain focus of the 5-m Hale telescope. The detectors are four 800 x 800 Texas Instrument CCDs covering a net field of $8'.7$ on a side with an image scale of $0''.335$ per pixel. The four CCDs image a contiguous 2×2 matrix of sky and the chips are oriented such that the readout directions of each detector are parallel. During the observations, the instrument was rotated such that the CCD columns were oriented north-south. Each drift scan was started by pointing the telescope at a position just south of the *Lockman* field, and then driving the telescope north across the field at a rate of $0'.90$ per min. The leading CCDs recorded the sky through the 'wide V' *F555W* filters employed in the HST Wide Field/Planetary Camera (cf. MacKenty et al. 1992), while near-infrared filters (*F785LP*; MacKenty et al. 1992) were placed in front of the trailing chips. The system response curves for these filters as well as the photometric properties are given in Postman et al. (1996).

The CCDs were operated in Time-Delay-and-Integrate (TDI) mode at a rate corresponding to the drift scan, resulting in an effective exposure of 293 s through each of the two filters. Except for the $\approx 2''$ gaps in the center of each scan caused by the 4-Shooter beam-splitter, the entire field

was covered with five drift scans whose centers were separated by 1.0 min in right ascension. The seeing FWHM was approximately $2''.5$. The initial processing of the drift scans followed the procedure described in Schneider et al. (1994). The scans were divided into a series of 816x800 images, with an 80 pixel overlap in the scan direction so every object of interest would be entirely contained in one frame. A bias level, calculated from the extended registers stored in the data, was subtracted from each frame, and a one-dimensional flat field was calculated for each detector by median filtering the data. Temporal variations in sky brightness, which appear as a change in background level in the scan direction, were removed from each frame by fitting third-order polynomials to the data.

Optical images were detected using the MIDAS package "inventory". The 3σ magnitude limit was around 23.5 in V and 22.5 in I. The object positions were corrected for overall systematic position errors along and across the scan path using the SKICAT scans of the POSS-II Schmidt plates (Weir et al. 1996). We estimate the astrometric accuracy to be better than $0.5''$.

3. Optical spectroscopy

Given the accuracy of the PSPC positions, which were the basis for the early phase of the identifications, and guided by the simulations described in Paper I, we considered any optical object within $15''$ from the position of the X-ray source as a potential identification. We named optical objects near the X-ray position A, B, ..., usually in order of increasing distance from the X-ray position. In a few cases, the X-ray position moved in subsequent analyses based on additional X-ray exposures, and optical objects farther in the alphabet became involved. For each X-ray source, spectra were obtained of optical candidates, more or less in order of brightness, until a probable identification was made (cf. Sect. 4). Finding charts and a full description of the spectra will be published elsewhere (Lehmann et al., in prep.).

3.1. Palomar spectra

Optical spectra for some of the brighter objects were obtained in February and December, 1992 with the 4-Shooter spectrograph (Gunn et al. 1987) at the 5-m Hale telescope. The spectrograph's entrance aperture is a $1.5 \times 100''$ slit and the detector an 800 x 800 Texas Instruments CCD. A 200 line mm^{-1} transmission grating produces spectra from 4500-9500Å at a spectral resolution of 25Å. The data were processed using the procedure given in Schneider et al. (1994). Several of the approx. 20 spectra taken showed that the objects were active galactic nuclei (AGNs), which at the time provided assurance that the celestial positions of the X-ray objects were approximately correct. Spectra for most of these objects were subsequently obtained with the Keck telescope (see below). For 10 objects (8B, 28B,

16A, 62A, 20A, 27A, 9A, 25A, 41C and 52A), the Palomar spectra are the basis for their entry in Table 1 (cf. Sect. 4). These include the three galactic stars among the X-ray sources.

3.2. Keck spectra

Spectra for all remaining optical objects were taken with the Low Resolution Imaging Spectrometer (LRIS) (Oke et al. 1995) at the cassegrain focus of the Keck 10-m telescope in February and December 1995, April 1996 and April 1997. The slit width is either $1''.0$ or $0''.7$ and the detector is a back-illuminated 2048×2048 Tektronics CCD. A 300 line mm^{-1} reflection grating produces spectra from $3800\text{--}8200\text{\AA}$ at a spectral resolution of around 10\AA . In order to minimize slit losses due to atmospheric selective refraction, we generally rotated the instrument so that the projection of the slit on the sky was vertical.

The raw data frames were bias-subtracted and flat-field corrected. The extraction of one-dimensional spectra from the two-dimensional sky-subtracted spectra was done using the optimal extraction algorithm for CCD spectroscopy described by Horne (1986). Third order polynomials were fitted to the lines of the He- Ar or Hg-Kr spectrum observed before or after the object spectrum to determine the wavelength scale. The flux calibration of the spectra was obtained using secondary standard stars for spectrophotometry (Oke & Gunn 1983). An atmospheric correction function for the broad molecular absorption bands (H_2O , O_2) was derived from the spectra of the standard stars and applied to all other spectra.

4. Optical identifications and source classifications

In this section, we define systematically the process followed in obtaining optical identifications of the X-ray sources. In order to facilitate this description, we introduce five identification classes (ID class), which categorize the process of identification and classification used in each class.

The primary goal is to obtain the optical identification of the X-ray source, i.e., the correct association of the X-ray source with an optical object. Once the identification has been made, the redshift of the X-ray source is obtained from that of the optical object. The classification of the source (star, galaxy, cluster of galaxies, AGN, etc.) is usually made on the basis of its optical properties. For some ID classes, we will also use the X-ray properties in classifying the source.

Since the surface density of optical objects that can be observed is much larger than that of the X-ray sources in our survey, the identification depends on finding an optical object within the X-ray error circle that has some unusual properties. In practice, we find for about half of the sources an optical object with broad emission lines, that we recognize as an AGN. We discuss these objects

below under ID classes $a - c$, and argue that AGNs are so rare that their detection near the X-ray source constitutes an almost certain identification of the X-ray source.

Among the remaining sources, we find optical objects with $[\text{Ne V}]$ or $[\text{Ne III}]$ emission (ID class d). We argue that $[\text{Ne V}]$ is indicative of soft X-ray emission, confirming the identification of the optical object with the X-ray source. For each of the two emission lines, we argue that they are rarely observed and confirm the optical identifications. On the basis of the Ne emission and the high X-ray luminosities, we classify the objects as AGNs.

For the remaining sources, we cannot find within the X-ray error circle optical objects with unusual properties (ID class e). For these sources we use the ratio of X-ray flux to optical flux f_x/f_v as additional tool in our classification procedure. This ratio is independent of distance and allows distinguishing different classes of X-ray sources (cf. Stocke et al. 1991). Once brighter optical objects (with smaller values of f_x/f_v) have been eliminated as candidate identifications, we find for most of the objects in ID class e that the ratio f_x/f_v is so large that the X-ray source cannot be a galaxy.

Clusters and groups of galaxies show approximately the same range of $\log f_x/f_v$ as AGNs (cf. Stocke et al. 1991). We do not see a rich cluster of galaxies on the CCD images at the position of most of the X-ray sources in ID class e . Therefore, among the known object classes typically associated with X-ray sources, they could in principle be AGNs or groups of galaxies. The intragroup medium in poor groups of galaxies has been identified as an important class of X-ray emitters through studies with ROSAT (Mulchaey et al., 1996). In these objects a small number of galaxies is surrounded by diffuse X-ray halos with a typical linear diameter of $50\text{--}400$ kpc and X-ray luminosities in the range $10^{42.5\text{--}43.5}$ erg s^{-1} . Often the peak of the X-ray emission is not centered on any one galaxy, but in some cases a cooling flow is centered on a dominant galaxy (see also Stocke et al., 1991). The local volume density of these groups (Henry et al., 1995) is large enough, that some higher redshift objects of this class are expected to show up in our survey. Similar objects at a redshift of 0.5 would have X-ray angular diameters (FWHM) of $10\text{--}50''$, and fluxes in the range $0.2 - 2 \times 10^{-14}$ $\text{erg cm}^{-2} \text{s}^{-1}$. The optical galaxies in these groups would often be seen at $\sim 10''$ from the centroid of the X-ray emission.

Table 1 provides a complete list of the X-ray sources of the survey and the properties of their optical identifications. The first two columns give the name of the X-ray source and its flux in units of 10^{-14} $\text{erg cm}^{-2} \text{s}^{-1}$ in the $0.5 - 2$ keV energy band (cf. Paper I). The next four columns give the name of the optical object identified with the X-ray source, its magnitude R , and its right ascension and declination at epoch 2000. The next column gives the distance of the optical object to the X-ray source in arcsec and indicates whether the X-ray position is mainly based on the 207 ksec PSPC pointing (P), the 1112 ksec HRI

Table 1. Photometric and spectroscopic properties of optical identifications of the X-ray sources^a

N_x	S_x	name	R	α_{2000}	δ_{2000}	Δ pos	$\log f_x/f_v$	G	z	M_V	$\log L_x$	class	ID class
28	19.90	28B	18.2	10 54 21.3	57 25 44.3	1 H	0.29	g	0.205	-22.0	43.59	AGN	c
8	11.84	8B	14.1	10 51 31.1	57 34 39.4	1 H	-1.58	s				star	dMe
6	8.82	6A	18.4	10 53 16.9	57 35 52.3	1 H	0.01	s	1.204	-25.6	44.89	AGN	a
32	6.50	32A	18.1	10 52 39.6	57 24 31.7	1 H	-0.24	s	1.113	-25.8	44.69	AGN	a
29	5.13	29A	19.5	10 53 35.1	57 25 41.6	1 H	0.22	s	0.784	-23.6	44.25	AGN	b
31	3.57	31A	20.0	10 53 31.8	57 24 53.8	0 H	0.26	s	1.956	-25.0	44.97	AGN	a
16	3.56	16A	19.8	10 53 39.8	57 31 03.9	1 H	0.18	s	0.586	-22.7	43.81	AGN	c
56	3.52	56D	18.9	10 50 20.2	57 14 21.7	1 R	-0.19	s	0.366	-22.6	43.37	AGN	b
62	3.20	62A	11.0	10 52 01.3	57 10 45.9	2 R	-3.39	s				star	FG
37	2.54	37A	19.6	10 52 48.2	57 21 17.4	2 H	-0.05	s	0.467	-22.4	43.46	AGN	b
20	2.43	20C	15.5	10 54 10.4	57 30 37.9	2 H	-1.71	s				star	dMe
9	1.88	9A	20.0	10 51 54.5	57 34 37.7	0 H	-0.02	g	0.877	-23.4	43.92	AGN	b
41	1.87	41C	17.9	10 53 18.7	57 20 43.9	5 H	-0.86	g	0.340	-23.4	43.03	Grp	e
25	1.84	25A	20.6	10 53 45.0	57 28 40.2	0 H	0.21	s	1.816	-24.3	44.61	AGN	a
42	1.69	42Y	20.7	10 50 16.1	57 19 53.8	7 P	0.22	s	1.144	-23.2	44.13	AGN	a
48	1.64	48B	19.9	10 50 46.2	57 17 33.1	1 R	-0.12	g	0.498	-22.3	43.33	AGN:	e
12	1.57	12A	22.9	10 51 48.8	57 32 48.4	1 H	1.06	s	0.990	-20.7	43.96	AGN	d
59	1.50	59A	16.9	10 53 24.8	57 12 30.7	5 P	-1.36	g	0.080	-21.3	41.63	AGN	c
35	1.48	35A	18.9	10 50 39.6	57 23 36.3	1 R	-0.56	s	1.439	-25.5	44.29	AGN	a
117	1.46	117Q	22.8	10 53 48.8	57 30 33.9	0 H	0.99	s	0.780	-20.3	43.70	AGN	d
27	1.39	27A	20.3	10 53 50.3	57 27 09.2	0 H	-0.03	g	1.720	-24.5	44.44	AGN	e
73	1.39	73C	20.6	10 50 09.6	57 31 43.5	14 P	0.09	s:	1.561	-24.0	44.34	AGN	a
52	1.32	52A	20.4	10 52 43.3	57 15 44.6	2 H	-0.01	s	2.144	-24.8	44.63	AGN	a
11	1.27	11A	23.0:	10 51 08.4	57 33 45.4	0 H	1.01	g	1.540	-21.5	44.29	AGN	a
67	1.24	67B	20.5:	10 50 56.2	57 06 47.9	8 P	-0.48	s	0.550	-21.9	43.29	Grp	e
26	1.20	26A	18.7	10 50 19.8	57 28 12.2	6 P	-0.73	g	0.616	-23.9	43.39	AGN	d
55	1.17	55C	21.4:	10 50 09.4	57 14 43.3	1 P	0.34	s:	1.643	-23.3	44.32	AGN	a
2	1.16	2A	20.1	10 52 30.1	57 39 13.4	2 H	-0.19	s	1.437	-24.3	44.18	AGN	a
54	1.12	54A	20.3	10 53 07.4	57 15 04.6	2 H	-0.12	s	2.416	-25.2	44.67	AGN	a
45	1.04	45Z	21.1	10 53 18.9	57 18 50.0	2 H	0.17	s	0.711	-21.8	43.46	AGN	d
19	0.99	19B	21.8	10 51 37.5	57 30 43.2	1 H	0.42	s	0.894	-21.6	43.66	AGN	b
504	0.96	51D	20.2	10 51 14.5	57 16 15.5	1 R	-0.23	s	0.528	-22.1	43.15	AGN	d
43	0.94	43A	23.0	10 51 05.1	57 19 23.2	2 R	0.88	s	1.750	-21.8	44.28	AGN	a
36	0.92				see text							-	e
46	0.89	46A	22.6	10 51 20.1	57 18 47.9	2 R	0.70	s	1.640	-22.1	44.20	AGN	a
61	0.79	61B	20.8	10 51 26.3	57 11 31.1	7 P	-0.07	g	0.592	-21.7	43.17	AGN	b
38	0.78	38A	21.3	10 53 29.5	57 21 03.9	2 H	0.12	s	1.145	-22.6	43.79	AGN	a
60	0.78	60B	21.6	10 52 48.5	57 12 06.0	3 P	0.24	g	1.875	-23.4	44.27	AGN	a
14	0.72				see text							-	e
47	0.71	47A	21.9	10 52 45.0	57 17 33.4	5 H	0.32	g	1.058	-21.9	43.68	AGN	a
30	0.70	30A	21.5	10 52 57.3	57 25 07.1	1 H	0.15	s	1.527	-23.0	44.02	AGN	a
51	0.66	51L	21.1	10 51 17.0	57 15 51.4	5 P	-0.03	s	0.620	-21.5	43.14	AGN	d
17	0.62	17A	20.3	10 51 04.0	57 30 54.0	2 H	-0.38	s	2.742	-25.4	44.54	AGN	a
814	0.61	37G	20.5	10 52 44.8	57 21 23.2	2 H	-0.31	s	2.832	-25.3	44.57	AGN	a
84	0.60				see text							-	e
77	0.59	77A	21.7	10 52 59.3	57 30 30.2	1 H	0.16	s	1.676	-23.0	44.04	AGN	a
53	0.58	53A	18.4	10 52 06.3	57 15 24.7	5 P	-1.17	g	0.245	-22.2	42.22	GAL	e
116	0.57				see text							-	e
23	0.56	23A	21.9	10 52 24.7	57 30 09.6	1 H	0.22	g	1.009	-21.8	43.53	AGN	b
58	0.56	58B	21.4	10 52 38.8	57 12 59.7	10 P	0.02	g	0.629	-21.3	43.08	Grp	e

^a For a description of the entries, cf. Sect. 3, and for a discussion of the ID classes, cf. Sect. 4.

4.2. ID class *d*

We use ID class *d* to cover objects that do not exhibit the emission features shown in ID classes *a*–*c*, but that show Ne emission lines. Four objects (12A, 117Q, 51D, and 51L) exhibit [Ne v] $\lambda 3426$ emission. Since the ionization potential of Ne⁺⁺⁺ is 97 eV, corresponding to soft X-ray emission, the presence of [Ne v] emission essentially confirms the optical identification of the X-ray source. (Among the objects of ID class *a*–*c* discussed above, we see [Ne v] emission in the spectra of four of them.) With the identification of the optical object confirmed and therefore the redshift of the X-ray source established, we find that the X-ray luminosity of all four sources is above 10^{43} erg s⁻¹, far higher than that of galaxies, and we conclude that they are AGNs.

Two objects (26A and 45Z) show relatively strong [Ne III] $\lambda 3869$ emission. This feature, although seen also in field galaxies with emission lines (cf. Hammer et al. 1997), is typically stronger in the spectra of quasars and Seyfert galaxies. Among the 10 AGNs of ID class *a*–*c* in which the [Ne III] emission is in the accessible spectral range, we see it in 7 cases. In all cases where we see [Ne v] emission, we also observe [Ne III] if it is accessible. Object 26A also exhibits Fe II $\lambda 2600$ absorption, which has been seen in spectra of broad absorption line quasars (Becker et al. 1997). We accept the two objects as the optical identifications, and then (as for the [Ne v] cases above) from the redshifts and the X-ray luminosities conclude that the objects are AGNs.

4.3. ID class *e*

In ID class *e*, we discuss the remaining objects that have galaxy counterparts without broad emission lines and without rare spectral features such as Ne emission lines. We have 10 objects with ID class *e* in Table 1, of which four exhibit [O II] emission. Claims have been made (Griffiths et al. 1996, McHardy et al. 1997) that a significant fraction of the weaker X-ray sources are narrow-emission line galaxies (NELG), characteristically showing strong [O II] $\lambda 3727$ emission, and that these constitute a new population of X-ray sources. Recent galaxy surveys have revealed that a large fraction of faint field galaxies show [O II] emission (cf. Hammer et al. 1997). Our own spectral work at Palomar and Keck has recorded spectra of 24 galaxies near the objects listed in Table 1 that have redshifts different from the optical identifications. Among these field galaxies, 19 exhibit [O II] emission, i.e., 79% of field galaxies are NELGs. The detection of a NELG can therefore not be taken as evidence for the correct identification of an X-ray source.

Since the optical spectra of possible X-ray counterparts in ID class *e* are undistinguished, we introduce two additional criteria by which to identify and classify the objects. The first criterion is the ratio of X-ray and optical

flux f_x/f_v which is independent of distance (cf. Stocke et al. 1991). In Fig. 2, we plot $\log f_x/f_v$ vs. the flux $S(0.5 - 2 \text{ keV})$ for the 37 AGNs of ID class *a*–*d* that we have identified so far, and for all AGNs and galaxies in the Extended Medium-Sensitivity Survey (EMSS, Stocke et al. 1991). Stocke et al. noted that essentially all AGNs in the EMSS are in the range $-1.0 < \log f_x/f_v < 1.2$. Among the 37 Lockman AGNs plotted, 36 have $\log f_x/f_v > -1.0$. There is no evidence from Fig. 2 for evolution of the f_x/f_v ratio of AGNs; for galaxies no or little effect of evolution would be expected given their relatively small redshifts.

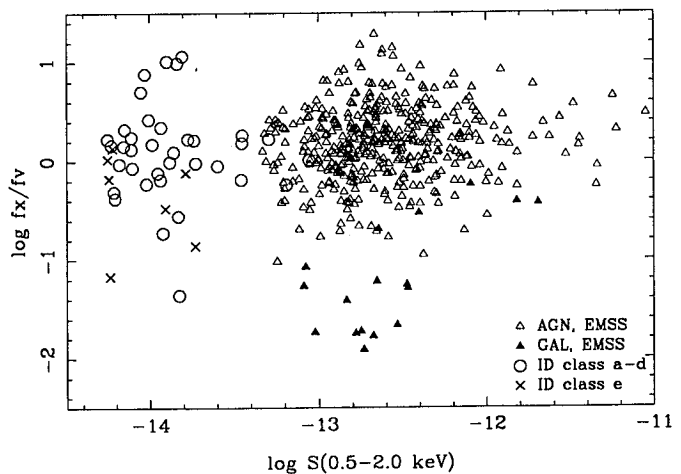


Fig. 2. Ratio of X-ray over optical flux plotted versus X-ray flux for Lockman and EMSS sources

The second criterion we considered is the angular extent of the X-ray emission. A rigorous determination of the X-ray extent for all sources has not been part of our analysis scheme because it breaks down in the presence of significant confusion (see Paper I). Therefore the extent has been estimated *a posteriori* for the objects in question by fitting a two-dimensional Gaussian to the HRI and PSPC images and comparing this to other nearby X-ray sources. Sizes are given in FWHM, approximately corrected for the size of the PSF. If a faint object is extended, it may be missed by the HRI observations, which are less sensitive for low surface brightness emission. On the other hand, the HRI may pick up some sharper structure within diffuse emission. Because of its softer response it is actually more sensitive to detect cooling flows. As noted before, optical galaxies in X-ray emitting poor groups would often be seen at positions outside the X-ray error circle. For an extended X-ray source we consider the detection of two or more galaxies at the same redshift as supporting the group identification.

In summary, while the X-ray emission from AGNs and single galaxies should be point-like and centered on the optical counterpart, clusters and groups of galaxies may have extended X-ray emission (and therefore reduced HRI fluxes relative to PSPC fluxes), that is displaced from one

or more galaxies. The discussion given below for each of the sources takes into account these additional criteria in order to illuminate whether it is more likely to be an AGN, a group of galaxies or something else.

Object 41 is extended by about $22''$ in both directions on the 1112 ksec HRI exposure and by $50''$ in the PSPC exposure. Optically, a dense group of galaxies is visible, of which 41C is the brightest member. Several other galaxies are at the same redshift as 41C. We classify the object as a group of galaxies, although it could be a cluster.

Object 48 is not extended in the PSPC exposure. It is seen as a point source in the HRI raster scan, well centered on the galaxy 48B but is not covered by the deep HRI pointing. Two other galaxies, at $9''$ and $85''$ from the X-ray source, have the same redshift as 48B. The object has a high $\log f_x/f_v$ ratio. Considering the excellent coincidence of the optical and the HRI position and the absence of evidence for an extent in X-rays, we consider 48B to be the optical identification. On the basis of its X-ray luminosity and f_x/f_v ratio, we classify this object as an AGN, although this classification has to be considered uncertain.

Object 27 is a complex case. The PSPC X-ray position is consistent with that of the optical quasar 27A. Early parts of the 1112 ksec HRI exposure show a source $10''$ SE of 27A but the more recent HRI exposures produce a source position less than $1''$ from 27A. Apparently, there are two variable sources involved. Since the survey is defined by the epoch of the PSPC observations, we identify the X-ray source with 27A.

Object 67 appears complex in the PSPC image. It is near the edge of the field, at $17.7''$ from the center. It is barely detected on the HRI raster scan, suggesting a substantial extension in X-rays. The galaxy 67B has $\log f_x/f_v = -0.48$. Three other galaxies in the error box have the same redshift as 67B. We classify the object as a group.

Object 36 is another case where variability plays a role. The source 36 is based on the PSPC exposures. The deep HRI survey shows an X-ray source (designated as number 870) about $15''$ to the south of 36. Near this position, we found the optical object 36F, which is an AGN at redshift 0.8, and clearly the identification. However, the HRI raster scan, which only recently produced accurate positions after an astrometrical solution provided by the ultradeep HRI pointing (see Paper I), clearly confirms the PSPC position and does not show an object near 36F. It thus appears that there are two X-ray sources and that 36F is strongly variable. Since, as stated, our survey is defined by the epoch of the PSPC observations, source 870 is not part of the current survey. We have resumed work to identify source 36, but it is incomplete so far.

Object 14 appears as a point source in both the PSPC and the 1112 ksec deep HRI exposures. The optical object nearest to the HRI position is a galaxy at a distance of $7''$. It has $R = 22.5$, $z = 0.546$, and its spectrum has no broad emission lines or Ne emission. The interpretation of this

object depends critically on whether it is strictly a point source or has an X-ray extension of, say, $20''$ that might well have escaped detection. If the source is extended, the galaxy might be a member of a group of galaxies that is the X-ray source. If on the other hand, the X-ray source is strictly a point source, then the galaxy is unlikely to be the identification: simulations discussed in Paper I show that the probability that an HRI point source of this X-ray flux would appear at a distance of $7''$ in our survey is around 2%. Since a Keck CCD-image shows that there is no object brighter than $R = 25$ in the HRI error circle, the single X-ray source would have $\log f_x/f_v > 1.6$, which would be truly outstanding. We cannot decide between a group of galaxies and an X-ray intense point source at the present time.

Object 84 appears to be a case similar to that of object 14. The PSPC and HRI images are probably not extended. Two galaxies at about $14''$ from the X-ray source have the same redshift. The spectrum of the brighter galaxy (84E, $R = 21.6$, $z = 0.525$) is illustrated in Fig. 1. There is no object in a deep R -band Keck image within the HRI error circle. The case for a group of galaxies is somewhat stronger here, since we do have two galaxies with the same redshift. On the other hand, if object 14 is a single object with large f_x/f_v then 84 might be another such case. We cannot decide between a group of galaxies and an X-ray intense point source at the present time.

Object 53A shows $H\alpha$ emission with $\text{FWHM} = 321$ km/sec consistent with instrumental broadening and it has $\log f_x/f_v = -1.17$. Accordingly, we classify the optical object as a galaxy. At the redshift of the galaxy, the X-ray luminosity ($\log L_x = 42.2$) is low for an AGN and rather high for a galaxy. The galaxy is located about midway between two bright M-type stars (neither of which is an important contributor to the X-ray emission).

Object 116 is extended by about $50''$ EW on the PSPC exposure. It is marginally seen on the 1112 ksec HRI exposure and probably extended. Three galaxies at distances of $3''$, $8''$ and $10''$ from the center of the PSPC error box, however, all have different redshifts (0.708, 0.408 and 0.610, respectively). We cannot present an optical identification at present.

Object 58 appears extended in the EW direction on the PSPC exposure, by about $40''$. The object is not detected on the 1112 ksec HRI exposure, consistent with its PSPC extent. At a distance of $14''$ from the PSPC position there is the galaxy 58B which has $\log f_x/f_v = -0.02$. Another galaxy at a distance of $11''$ from the center of the error box is at the same redshift. We classify the object as a group of galaxies.

5. Comparison with other ROSAT PSPC surveys

Several medium and deep surveys conducted with the PSPC on board ROSAT have been published in the past several years. We are interested in comparing our results

Table 2. Comparison of ROSAT PSPC surveys

Survey ^a	Area ^b	T ^c	S_{lim}^d	N^e	AGN	GAL	unid.	FC ^f	FL ^g	FU ^h
CRSS	3.9	>6	2.0	123	55%	10%				
DRS	1.4	21 49	0.3	194	55%	10%	18%	8%	38%	13%
NEP	0.2	79	1.0	20	65%	0%	10%	5%	4%	5%
UKDS	0.2	110	0.2	70	46%	26%	16%	8%	41%	26%
RDS	0.3	207	0.5	50	78%	2%	8%	6%	8%	5%

^a cf. text for explanation of acronyms

^b approximate, in square degrees

^c PSPC exposure time, in ksec

^d limiting flux $S(0.5 - 2\text{keV})$ in units of $10^{-14} \text{ erg cm}^{-2} \text{ s}^{-1}$

^e number of X-ray sources detected

^f fraction of output sources that are contaminated, based on simulations

^g fraction of input sources that are lost, based on simulations

^h fraction of output sources that are unidentifiable, based on simulations

with those surveys in which optical identification and spectroscopy have been carried out for the majority of the detected X-ray sources. These are:

- The Cambridge-Cambridge ROSAT Serendipity Survey (CRSS, Boyle et al. 1995)
- A deep ROSAT survey (DRS, Georgantopoulos et al. 1996)
- The ROSAT North Ecliptic Pole Deep Survey (NEP, Bower et al. 1996)
- The UK ROSAT deep field survey (UKDS, McHardy et al. 1997)

We list in Table 2 the properties of the surveys (the present survey is denoted as RDS), as well as the fractions identified as AGNs and galaxies. In general, the area covered by a given survey varies with limiting flux. The limiting fluxes S_{lim} given in Table 2 are those mentioned in the quoted references and generally refer to the weakest X-ray sources in the sample.

The fraction of sources identified as AGNs in the RDS is larger than that in all other surveys. This is partly due to the high quality of the Keck LRIS spectra and partly due to our classification procedure. In particular, we have used evidence based on the presence of [Ne V] or [Ne III] emission, together with the high X-ray luminosity to classify 6 objects (12%) as AGNs that otherwise might have been classified as galaxies.

We can carry out a direct comparison of the RDS with the two shallower surveys. Based on the CRSS AGN and galaxy percentages, we would expect to find among the 11 RDS sources above $2 \cdot 10^{-14} \text{ erg cm}^{-2} \text{ s}^{-1}$ six AGNs and one galaxy, whereas we observe eight AGNs and no galaxies. Similarly, based on the NEP AGN percentage, we would expect in the RDS above $10^{-14} \text{ erg cm}^{-2} \text{ s}^{-1}$ 20 AGNs, whereas we observe 25. We conclude that the percentages of AGN and galaxies for the CRSS, the NEP and the RDS are not significantly different.

The DRS and the UKDS have lower quoted limiting fluxes than the RDS, even though their exposure times are shorter. Given the simulations discussed in Paper I, this raises concerns about the effects of confusion. We show in Table 2 the three F-factors derived from simulations relevant to the different surveys, as described in Paper I. The contamination factor FC represents the fraction of output sources that have a flux in excess of 1.5 times the nearest input source (if within $15''$) augmented by 3σ . In practice, more than half the photons of these output sources did not originate from the nearby input source. The loss factor FL is the fraction of input sources that do not have an output source within $10 - 15''$. These input sources are not detected at all or have lost their identity and in practice cannot be optically identified. The factor FU is the fraction of output sources that has no input source within $15''$. It therefore represents the unidentifiable fraction of the detected sources.

The loss factors FL for the DRS and the UKDS show that 38 and 41%, respectively, of the input sources (i.e., the real sources in the field) are lost. In contrast, the NEP and the RDS lose only 4 and 8% of the input sources. Actually, since in the RDS the 1112 ksec HRI survey covers about $2/3$ of the $R < 12'5$ PSPC field, the effective values of FC and FL are less than those given in Table 2.

Among the sources that are detected, the factor FU for the UKDS suggests that 26% should be unidentifiable. McHardy et al. (1997) state that 11 out of 70 sources, or 16%, are unidentifiable. The discrepancy between these two percentages raises the question whether some of the unidentifiable sources in the UKDS may have been identified incorrectly. We suspect that this is the case, and that the misidentifications involve the NELGs which are claimed to be a new population of X-ray sources (Griffiths et al. 1996, McHardy et al. 1997). As discussed in Sect. 4.3, NELGs make up such a large fraction of faint field

galaxies that the presence of a NELG in the X-ray error circle cannot be taken to confirm its identification of the X-ray source.

6. Discussion and conclusion

Our procedure to identify and classify the weak X-ray sources in the RDS depends on the angular extent of the object. For stars and AGNs (cf. ID classes *a* – *d*) which are point sources both in X-rays and optically, we require positional agreement between the X-ray and the optical source. As can be seen for the objects of ID class *a* – *d* in Table 1, the average offset between X-ray and optical positions is 6'' for PSPC positions and less than 2'' for HRI positions. Identifications are based, first on the presence of broad emission lines, second on the combination of the presence of [Ne V] emission and high X-ray luminosity, and third on the presence of relatively strong [Ne III] emission. We argue that the presence of one or more broad emission lines in the spectrum of an optical object near the X-ray source signifies an AGN, and that these are sufficiently rare that this essentially confirms the identification. The presence of [Ne V] is taken to be indicative of soft X-ray emission, confirming the optical object as the identification of the X-ray source, and the high X-ray luminosity derived from the redshift signifies an AGN. Given the rare occurrence of strong [Ne III] emission, its presence is also considered to confirm the identification.

For the remaining 10 objects, of ID class *e*, the identification procedure is quite different. Many of these objects have extended X-ray emission and some have a low HRI flux or a positional offset between HRI and PSPC. X-ray variability is seen in two cases, complicating the identification procedure. Generally, the ratio f_x/f_v is fairly large, suggesting that the object is an AGN or a group or cluster of galaxies. We take evidence for X-ray source extension and the presence of several galaxies at the same redshift as suggestive of identification with a group of galaxies, even though we have not systematically explored galaxies near the X-ray source.

Applying these classification rules, we find 39 AGNs, 3 groups of galaxies, 1 galaxy and 3 stars. Among the AGNs, 16 have $M_V < -23.3$, corresponding to $M_B < -23.0$ which according to the luminosity criterion of Schmidt & Green (1983) would qualify them as quasars, while the other 23 AGNs according to their optical luminosities are Seyfert galaxies. Among the four sources that remain unidentified, the observations for object 36 are not complete, while source 116 is most likely a group of galaxies. The most intriguing X-ray sources are objects 14 and 84, for which there is no evidence for source extension and where the ratio $f_x/f_v > 40$, larger than any shown in Fig. 2. However, if these sources have modest extension that could have remained undetected so far, they could still be groups of galaxies, as discussed in Sect. 4.3.

Roche et al. (1995), Shanks et al. (1996) and Almaini et al. (1997) find evidence for a significant cross-correlation between $B < 23$ galaxies and weak unidentified X-ray sources. Almaini et al. find that $B < 23$ galaxies account for 23% of the X-ray background at 1 keV. This finding is qualitatively consistent with the substantial fraction of AGNs which are morphologically classified as galaxies in our survey (see Table 1). Further analysis is required to understand the relationship between these results in detail.

The fraction of X-ray sources with reliable optical identifications and redshifts in the RDS is higher than that in any previously published X-ray survey. This is a consequence of the realistic X-ray flux limits we used based on simulations, the role of deep HRI exposures for many of the sources in the central part of the PSPC field and the high quality of most of the Keck spectra obtained with LRIS. While the survey is based on sources selected above given flux limits based on PSPC exposures, the effect of the subsequent HRI imaging was considerable. In the early phase of the identification work, X-ray positions were based on PSPC images. In most cases, the identifications obtained were confirmed later by the much more accurate HRI positions. In two cases, the HRI managed to resolve confusion in the PSPC image, resulting in each case in an object pair, 37A+37G and 51D+51L, respectively. The HRI exposures also played a significant role in the realization that a number of X-ray sources are not associated with single objects but rather are possible groups of galaxies (e.g., object 58), either by directly confirming their extent or showing an offset between X-ray and optical positions.

We discuss claims in the literature for the appearance of a new population of weak X-ray sources in the form of narrow-emission line galaxies (NELG). We note that these claims are made on the basis of surveys that according to our simulations are strongly affected by confusion, leading to a substantial number of detected sources that are unidentifiable. Given that a large percentage of faint field galaxies are actually NELGs, we suggest that some of the unidentifiable sources identified as NELG are field galaxies that have no relation to the X-ray source. We do not claim that there cannot exist a new population among the weaker X-ray sources. Given the natural uncertainties that accompany the identification of objects of ID class *e*, such a new population could only be found in surveys with conservative flux limits in which confusion plays a minor role.

We will address in a subsequent communication the luminosity functions of the extragalactic X-ray sources and the origin of the X-ray background at energies below 2 keV.

Acknowledgements. The ROSAT project is supported by the Bundesministerium für Forschung und Technologie (BMFT), by the National Aeronautics and Space Administration (NASA), and the Science and Engineering Research Council

(SERC). The W. M. Keck Observatory is operated as a scientific partnership between the California Institute of Technology, the University of California, and the National Aeronautics and Space Administration. It was made possible by the generous financial support of the W. M. Keck Foundation. We thank the Institute for Astronomy of the University of Hawaii, Palomar Observatory, and the National Optical Astronomy Observatories for grants of observing time. We thank Bev Oke and Judy Cohen for their efforts in the construction of LRIS. E. Wyckoff and B. McLean for assistance in the photometric and astrometric reduction of the CCD images taken with the University of Hawaii 2.2 m telescope, and R. de Carvalho and G. Djorgovski for providing us with data from the POSS-II catalogue in our field. We thank an anonymous referee for carefully reading the manuscript and suggesting important improvements. M.S. thanks the Alexander von Humboldt-Stiftung for a Humboldt Research Award for Senior U.S. Scientists in 1990-91; and the directors of the Max-Planck-Institut für extraterrestrische Physik in Garching and of the Astrophysikalisches Institut Potsdam for their hospitality. This work was supported in part by NASA grants NAG5-1531 (M.S.), NAG8-794, NAG5-1649, and NAGW-2508 (R.B. and R.G.), NAG5-1538 and NAG8-1133 (R.B.), and NSF grants AST86-18257A02 (J.G.) and AST95-09919 (D.S.). G.H. acknowledges the DARA grant FKZ 50 OR 9403 5. G.Z. acknowledges partial support by the Italian Space Agency (ASI) under contract ASI 95-RS-152.

References

- Almaini O., Shanks T., Griffiths R.E., et al., 1997, MNRAS submitted (astro-ph/9704117)
- Becker R., Gregg M.D., Hook I.M., et al., 1997, ApJ 479, L93
- Bower R.G., Hasinger G., Castander F. J., et al., 1996, MNRAS 281, 59
- Boyle B.J., McMahon R.G., Wilkes B.J., Elvis M., 1995, MNRAS 272, 462
- Chevalier C., Ilovaisky S.A., 1991, A&AS, 90, 225
- De Ruiter H.R., Zamorani G., Parma P., et al., 1997, A&A 319, 7
- Georgantopoulos I., Stewart G.C., Shanks T., et al., 1996, MNRAS 280, 276
- Giacconi R., Gursky H., Paolini F.R., et al., 1962, Phys. Rev. Lett. 9, 439
- Griffiths R.E., Della Ceca R., Georgantopoulos I., et al., 1996, MNRAS 281, 71
- Gunn J.E., Carr M.L., Danielson G.E., et al., 1987, Opt. Eng. 26, 779
- Hasinger G., Burg R., Giacconi R., et al., 1993, A&A 275, 1
- Hasinger G., Burg R., Giacconi R., et al., 1997, A&A in press (Paper I)
- Hammer F., Flores H., Lilly S.J., et al., 1997, ApJ 481, 49
- Henry J.P., Gioia I.M., Huchra J.P., et al., 1995, ApJ 449, 422
- Horne K., 1986, PASP 98, 609
- Lockman F.J., Jahoda K., McCammon D., 1986, ApJ 302, 432
- MacKenty J.W., Griffiths R.E., Sparks W.B., et al., 1992, "Wide Field Planetary Camera Instrument Handbook (Version 3.0)", Space Telescope Science Institute Pub.
- McHardy I.M., Jones L.R., Merrifield M.R., et al., 1997, MNRAS submitted (astro-ph/9703163)
- Mulchaey J.S., Davis D.S., Mushotzky R.F., Burstein D., 1996, ApJ 456, 80
- Oke J.B., Cohen J.G., Carr M., et al., 1995, PASP 107, 375
- Oke J.B., Gunn J.E. 1983, ApJ 266, 713
- Postman M., Lubin L.M., Gunn J.E., et al., 1996, AJ 111, 615
- Roche N., Shanks T., Georgantopoulos I., et al., 1995, MNRAS 273, L15
- Schmidt M., Green R.P., 1983, ApJ 269, 352
- Schneider D.P., Schmidt M., Gunn J.E., 1994, AJ 107, 1245
- Shanks T., Almaini O., Boyle B.J., et al., 1996, in: Zimmermann H.U., Trümper J.E., Yorke H. (eds.) Röntgenstrahlung from the Universe, MPE Report 263, 341
- Stoche J.T., Morris S.L., Gioia I.M., et al., 1991, ApJS 76, 813
- Valdes F., 1982, FOCAS Users Manual (Tucson, NOAO)
- Weir N., Fayyad U.M., Djorgovski S.G., et al., 1995, PASP 107, 1243
- Zamorani G., 1995, in: Walsh J.R., Danziger I.J. (eds.) Science With VLT, ESO Ap. Symp., Springer, Berlin, p. 402
- Zitelli V., Mignoli M., Zamorani G., Marano B., Boyle B.J., 1992, MNRAS 256, 349